THESIS

TOPOGRAPHIC AND DIURNAL INFLUENCES ON STORMS ASSOCIATED WITH HEAVY RAINFALL IN NORTHERN COLORADO

Submitted by

Zoe A. Douglas

Department of Atmospheric Science

In partial fulfillment of the requirements

For the Degree of Master of Science

Colorado State University

Fort Collins, Colorado

Spring 2024

Master's Committee:

Advisor: Kristen L. Rasmussen

Michael M. Bell
Stephanie K. Kampf

ABSTRACT

TOPOGRAPHIC AND DIURNAL INFLUENCES ON STORMS ASSOCIATED WITH HEAVY RAINFALL IN NORTHERN COLORADO

Despite its profound impacts on agricultural and socioeconomical conditions globally, heavy rainfall is a high-impact weather phenomenon of which we have limited quantitative understanding and forecast skill. The Prediction of Rainfall Extremes Campaign in the Pacific (PRECIP) planned to observe the spectrum of heavy rainfall events in the moisture-rich environment of Taiwan and Japan during 2020, but was delayed until 2022 due to the global COVID-19 pandemic. As a result of this unanticipated delay, the PRECIP science team conducted the Preparatory Rockies Experiment for the Campaign in the Pacific ("PRE"-CIP), which observed precipitation over northern Colorado from May to August 2021 using Colorado State University's ground-based research radars and radiosondes. Extreme precipitation features are identified in the radar data and organized into storm modes based on prior research on the Tropical Rainfall Measuring Mission satellite's Precipitation Radar. An "ingredients-based" approach provides a theoretical framework to separate the storm modes into a spectrum of storm intensity and duration during the entire "PRE"-CIP field project, allowing us to connect storm modes to the topography, diurnal cycle, and overall rainfall characteristics in northern Colorado.

While precipitation occurred from the mountains to the plains, the highest concentration of storm tracks calculated from all ground-based radar observations occurred over the Rocky Mountains, regardless of storm duration. The majority of storm tracks are of low intensity and short duration, with over 80% of tracked storms having lifetimes of 1 h or less, suggesting that the general population of warm-season precipitation in northern Colorado is short-lived and of weak intensity. When considering heavy rainfall-producing storms, deep convection is the most dominant storm mode in northern Colorado by up to three orders of magnitude over broader convective and

stratiform systems. Deep convection most frequently occurred over the Rocky Mountains in the afternoon, whereas broader convective and stratiform systems most frequently occurred over the foothills and plains in the evening to nighttime hours. Therefore, diurnal forcing and orographic lift play important roles in the morphology of warm-season precipitation in northern Colorado, as has been seen in mountainous regions across the world. The frequent occurrence of deep convective storms directly over the Rocky Mountains, however, differs from the deep convective hotspots seen in the lowlands downstream of similarly large mountain barriers like the Andes and Himalayas. Ultimately, these radar-based analyses are important for the eventual comparison of heavy rainfall in a semi-arid midlatitude region (Colorado) and a moisture-rich tropical environment (Taiwan and Japan), thus providing an enhanced global understanding of the commonalities of heavy rainfall processes.

ACKNOWLEDGEMENTS

I would like to thank my advisor Kristen Rasmussen for her guidance and feedback over the last two and a half years. It has been a pleasure working with her, and I look forward to more years together during my Ph.D. program. I would also like to thank my committee members Michael Bell and Stephanie Kampf for their discussions regarding this manuscript. I am grateful for the PRECIP orographic team's helpful comments and suggestions over the years, and I look forward to diving into the PRECIP 2022 data with them during my Ph.D. work.

I appreciate the Rasmussen research group members, both past and present, for their camaraderie and support as we all tackle graduate school together. I would like to thank one Rasmussen group member in particular, Marqi Rocque, for providing me with the storm mode scripts that kick-started this M.S. research. I would also like to thank CSU alumni and University of Alabama in Huntsville professor Sean Freeman for his assistance with understanding and debugging my tobac scripts.

I would like to thank my friends and family, especially my parents Steven and Vicki Douglas, for their endless support of my passion for atmospheric science since I was in elementary school. The biggest thank-you goes to my partner Nicolas Gordillo for not only trouble-shooting my buggy scripts countless times, but also his unconditional love and comforting hugs over the last two years.

This research was funded by NSF Grant AGS-1854399.

DEDICATION

To Sophie, my canine best friend for nearly 14 years. Thank you for joining me in Colorado and being the best working-from-home partner.

TABLE OF CONTENTS

LIST OF FIGURES

Chapter 1

Introduction

Heavy rainfall is a high-impact weather phenomenon that significantly impacts socioeconomical and agricultural conditions globally, yet our fundamental understanding and forecast skill of heavy rainfall events remains limited. In response to the difficulties of operational flash flood forecasting in the U.S., Doswell et al. (1996) developed a physically based framework for forecasting heavy rainfall regardless of region. This methodology invokes a simple concept attributable to C. F. Chappell, in which "the heaviest precipitation occurs where the rainfall rate is the highest for the longest time" (Doswell et al. 1996). In mathematical terms, this concept is notated as

$$P = I \times D, \tag{1.1}$$

in which P is the rainfall accumulation, I is the rainfall intensity, and D is the duration of a storm. Storm intensity is often represented as an instantaneous rain rate, which can only occur if moist air is lifted to its condensation level. Therefore, I must be proportional to the vertical moisture flux wq, in which w is vertical velocity and q is specific humidity. This proportionality is determined by precipitation efficiency E, which is the ratio of water vapor precipitating out of the storm to the influx of water vapor into the storm. These atmospheric "ingredients" all contribute to rainfall intensity such that $I = Ewq$ (Doswell et al. 1996). That is, significant rain rates are achieved when rising air possesses substantial moisture, rapidly ascends into a storm, and experiences minimal dry-air entrainment. Similarly, the longest storm durations result from slow storm movement speeds and large precipitation areas. This area can be represented by the length scale of the storm system L, and duration is maximized when storm motion C is slow along this length scale, which is mathematically notated as $D = L/C$ (Doswell et al. 1996). Given that these

ingredients contribute to storm intensity and duration, Equation 1.1 can be rewritten as

$$P = (Ewq)(L/C), \tag{1.2}$$

which is the ingredients-based methodology for forecasting heavy rainfall (Doswell et al. 1996).

This ingredients-based methodology can be applied to not only flash flood forecasting, but also the characterization of rainfall observations in general. Using the polar-orbiting Tropical Rainfall Measuring Mission (TRMM) satellite's Precipitation Radar (PR), Zipser et al. (2006) and Houze et al. (2015) found that the regions with the deepest storms do not typically overlap with regions that experience the most rainfall. This result suggests that a spectrum of storm modes spanning different vertical and horizontal scales is necessary for characterizing heavy rainfall on a global scale. These storm modes include deep convective cores (DCCs), wide convective cores (WCCs), deep and wide convective cores (DWCCs), and broad stratiform regions (BSRs). DCCs are associated with young, vigorous convection and have been found to occur downstream of the Himalayas (Houze et al. 2007; Romatschke et al. 2010) and Andes (Romatschke and Houze 2010; Rasmussen and Houze 2011; Rasmussen et al. 2016), where dry, downsloping mountain air converges with moist low-level flow in the lowlands. BSRs are associated with mature mesoscale convective systems (MCSs) and have been found to occur most often over oceanic and maritime continental environments, where BSRs coincide with a maximum in MCS occurrence and thus the overall rainfall maximum (Houze et al. 2007; Romatschke et al. 2010; Romatschke and Houze 2010; Rasmussen and Houze 2011; Houze et al. 2015; Rasmussen et al. 2016). WCCs and DWCCs fall somewhere in between these two precipitation extremes and often, but not always, act as an intermediary as DCCs weaken and grow upscale into BSRs, particularly in subtropical South America (Romatschke and Houze 2010; Rasmussen and Houze 2011; Houze et al. 2015; Rasmussen et al. 2016).

Although the occurrence of intense convection is associated with the topography in South Asia and subtropical South America, Zipser et al. (2006) note that this connection to the topography is less clear for the region of the U.S. east of the Rocky Mountains, another hotspot identified

by the TRMM PR. Dedicated to studying tropical rainfall, TRMM PR observations are bounded between 35°N and 35°S, so the TRMM PR did not observe precipitation over the Colorado Rocky Mountains, whose southern border is defined by 37°N, and U.S. states further north. Nevertheless, Zipser et al. (2006) expanded the TRMM PR domain to 60°N and 60°S using the polar-orbiting F-14 satellite, showing that only the north-central U.S. matches the southeastern U.S. in storm intensity. The north-central U.S. is home to the Great Plains, where MCSs have a nocturnal summertime maximum and contribute to at least 60% of the warm-season rainfall within the region (Fritsch et al. 1986; Haberlie and Ashley 2019; Schumacher and Rasmussen 2020). This nocturnal MCS maximum is driven by the convergence of dry, diurnally cooled, downsloping Rocky Mountain air with the Great Plains low-level jet (LLJ), a nocturnal low-level southerly wind maximum that transports warm, moist air from the Gulf of Mexico (Bonner 1968; Mitchell et al. 1995).

While the Rocky Mountains are critical for downstream MCS development, they are also capable of initiating storms over the high terrain through mechanisms such as orographic lifting, leeside convergence, and wake effects (Banta and Schaaf 1987). East-west ridges such as the Palmer Divide and Cheyenne Ridge along the Front Range of the Rocky Mountains provide local confluence midday, thereby creating a preferred location for convective initiation in northern Colorado (Toth and Johnson 1985). Model simulations and observations have also indicated the presence of a mountain-plains solenoid in the Rocky Mountains, a thermally driven west-to-east circulation that supports daytime convection over the mountains and evening to nighttime convection over the plains (Toth and Johnson 1985; Tripoli and Cotton 1989a,b; Wolyn and McKee 1994; Trier et al. 2010).

One of the largest impacts of heavy rainfall-producing storms is flooding, which is one of the deadliest weather-related hazards in the U.S., second only to heat (Ashley and Ashley 2008). Flooding is well documented within the Colorado Front Range, with three deadly floods having occurred in the last five decades: the Big Thompson flood of 1976, the Fort Collins flood of 1997, and the Great Colorado Flood of 2013. As much as 10 in. of rain fell in the Big Thompson River drainage on the evening of 31 July 1976, claiming at least 139 lives and $35.5 million in damages

(Maddox et al. 1978; Caracena et al. 1979). A maximum of 10.2 in. was recorded during the Fort Collins flood on 28 July 1997, which resulted in 5 fatalities, exceeded $200 million in damages, and broke the 1-day, 6-h, and 3-h rainfall accumulation records at the Colorado State University weather station (Petersen et al. 1999). The Great Colorado Flood along the Front Range occurred from 9-16 September 2013, claiming 8 lives and resulting in over $2 billion in damages. Many locations saw up to 8 in., with over 15 in. recorded in some areas (Gochis et al. 2015). All three events were characterized by anomalously high moisture content and low-level upslope flow (Maddox et al. 1978; Caracena et al. 1979; Petersen et al. 1999; Gochis et al. 2015), which are important in the ingredients-based framework (Doswell et al. 1996).

Even though intense convection and flooding due to heavy rainfall is well documented along the Front Range, no study has examined the morphology of heavy rainfall-producing storms within the region. One of the primary science objectives of the Prediction of Rainfall Extremes Campaign in the Pacific (PRECIP) was to observe heavy rainfall-producing storms in the moisture-rich environment of Taiwan and Japan, but was delayed from 2020 to 2022 due to the global COVID-19 pandemic. This unanticipated delay allowed the PRECIP science team to conduct a complementary field project between May and August 2021 in Colorado, the Preparatory Rockies Experiment for the Campaign in the Pacific ("PRE"-CIP). For these two field experiments, the PRECIP science team designed an intensity-duration "phase space" that combines the Doswell et al. (1996) ingredients-based methodology with the spectrum of heavy rainfall-producing storms, as shown in Figure 1.1. The TRMM-heritage storm modes occupy different regions of this phase space: DCCs represent high-intensity, short-duration storms; BSRs represent low-intensity, long-duration storms; and DWCCs and WCCs are located in between these extreme corners of the phase space. To observe heavy rainfall in northern Colorado, the PRECIP science team utilized Colorado State University's ground-based research radars, atmospheric soundings, and Micro-Pulse Differential Absorption Lidars (MicroPulse DIALs, or MPDs).

Chapter 2 specifies how radar reflectivity data from "PRE"-CIP is used for precipitation tracking and storm mode identification in northern Colorado, as well as how global reanalysis data is

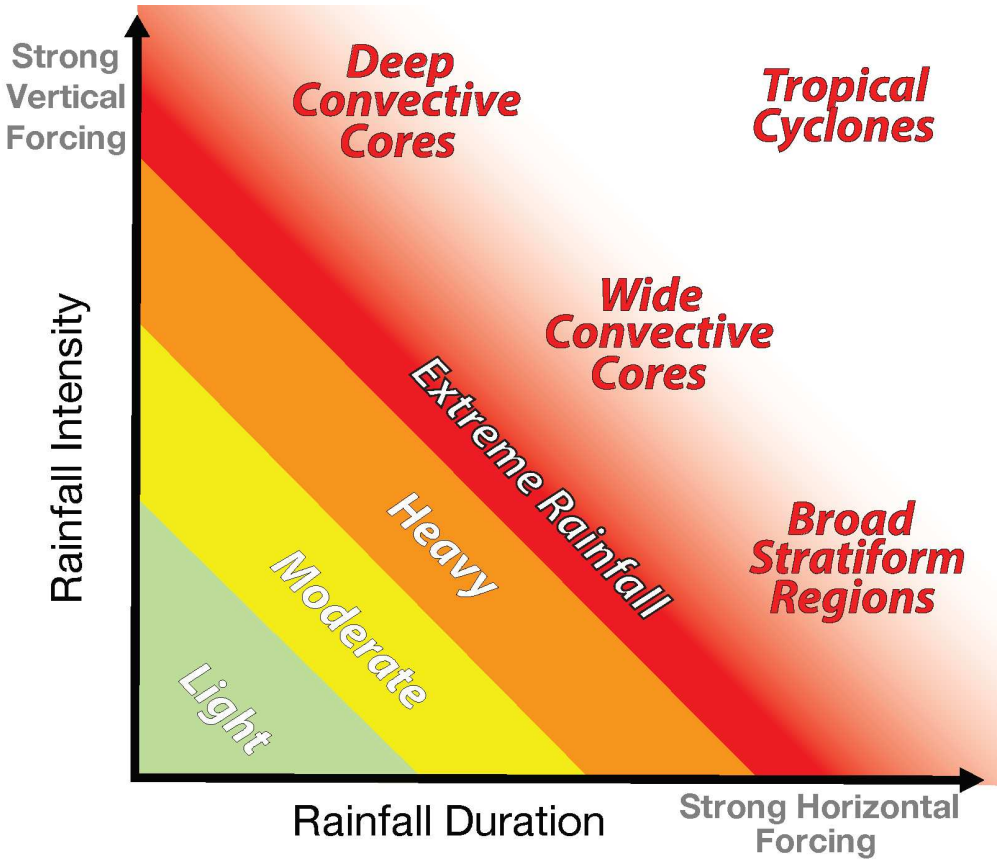

Figure 1.1: Schematic of the intensity-duration phase space based upon the ingredients-based framework of Doswell et al. (1996). The TRMM-heritage storm modes occupy the upper right corner of the phase space, where high-intensity and/or long-duration storms produce heavy, or extreme, rainfall. Figure is reproduced from the PRECIP science website (http://precip.org/science/).

used to investigate the synoptic-scale environment during the field project. Chapter 3 explores the overall synoptic conditions and their relationships with the topography and diurnal cycle, while Chapter 4 considers how these synoptic conditions explain the radar-observed rainfall. Chapter 5 describes the results of storm tracking in terms of the location, intensity, and duration of all observed precipitation, while Chapter 6 investigates the topographic and diurnal influences on the TRMM-heritage storm modes associated with heavy rainfall. Chapter 7 discusses the conclusions and future work.

Chapter 2

Data and Methodology

2.1 ERA5 Data

To understand the synoptic environment over the northern Colorado region during "PRE"-CIP, this study uses fifth-generation European Centre for Medium-Range Weather Forecasts (ECMWF) reanalysis (ERA5) data at 0.25° × 0.25° horizontal grid spacing (Hersbach et al. 2022). Specifically, we use monthly averaged data for May through August 2021 at 850 hPa to capture the low-level specific humidity, meridional wind, and vertical moisture flux. This monthly averaged data is partitioned by each hour of the day (e.g., average specific humidity values during May at 00 LT, 01 LT, 02 LT, etc.), allowing us to explore the influence of the diurnal cycle on the observed precipitation. Finally, anomalies of specific humidity, meridional wind, and vertical moisture flux are calculated by compositing the mean values of these atmospheric ingredients from 1979 to 2020 and then subtracting this historical mean from the 2021 values. These variables and their anomalies are investigated within the domain of 37°N to 43°N and 100°W to 110°W, which includes the entire state of Colorado as well as parts of the neighboring states of Kansas, Nebraska, Utah, and Wyoming. Expanding the ERA5 domain beyond that of the field project's C-band radar allows for a larger-scale analysis of the synoptic environment, which produced storms that both initiated within and moved into the radar domain. Furthermore, we can investigate the influences of the Great Plains LLJ by extending the domain into Kansas and Nebraska, where the wind speeds of the LLJ are maximized overnight (Bonner 1968; Mitchell et al. 1995).

2.2 Radar Data

The radar data used in this study is the penultimate, quality-controlled dataset from the primary research radar deployed during "PRE"-CIP, the Colorado State University C-band Instrument for Hydrological Volumetric Observation (CSU-CHIVO, hereafter CHIVO). Located in northeast-

ern Fort Collins, CO, CHIVO is closer to the Rocky Mountains than the operational National Weather Service (NWS) Weather Surveillance Radars–1988 Doppler (WSR-88Ds) in Denver, CO, and Cheyenne, WY. CHIVO's proximity to the Rockies allows the radar to observe storms over the mountains at lower atmospheric levels than the NWS WSR-88Ds, thereby providing a more complete view of high-terrain storms. While another research radar operated during "PRE"-CIP, the Colorado State University–University of Chicago–Illinois State Water Survey (CSU-CHILL) radar is excluded from this analysis since it did not begin operations until mid-July, two and a half months into the field project. The data from CHIVO was corrected for attenuation and speckle noise, and non-weather echoes were censored. Bad data was removed based on extreme thresholds of signal-to-noise ratio (SNR), signal quality index (SQI), and correlation coefficient. Rain rates were estimated using the default reflectivity–rain rate (Z-R) relationship used operationally by the NWS WSR-88Ds:

$$Z_h = 300R^{1.4}, \tag{2.1}$$

where Z_h is the horizontal reflectivity factor in units of mm^6 m^{-3} and R is the rain rate in mm h^{-1}.

Equation 2.1 is recommended for application during deep summertime convection in the mid-latitudes and is considered a good compromise between stratiform and convective rainfall. However, Z-R relationships tend to overestimate rainfall in high-reflectivity cores due to the dependence of reflectivity on a drop-size distribution. In future work, we will replace the Z-R relationship with a blended algorithm that considers two polarimetric radar variables—differential reflectivity (Z_{DR}) and specific differential phase (K_{DP})—in addition to Z_h for estimating rainfall (Cifelli et al. 2011). Such a blended, or hybrid, rainfall algorithm utilizes the strengths of different rainfall estimators in different precipitation scenarios and has been tested against three heavy rainfall and hail events in Colorado, a high-plains environment where ice contamination can heavily influence drop-size distributions (Cifelli et al. 2011). The hybrid algorithm's introduction of hydrometeor information improved the rainfall estimation over the standard Z-R relationship, which is promising for estimating heavy rainfall with the "PRE"-CIP radar data.

CHIVO's 12-minute scanning strategy included both range-height indicator (RHI) and surveillance (SUR) scans, although we are only considering the SUR scans for the purposes of this study due to the lack of horizontally continuous information in RHI scans. The mandatory SUR scan, SUR1, ran for approximately 4 min and 40 s and scanned at the 0.5°, 1.0°, 1.5°, 2.0°, 3.0°, 4.0°, 5.0°, 7.0°, 9.0°, 11.0°, 13.0°, and 15.0° elevation angles. A secondary SUR scan, SUR2, ran for approximately 3 min and 40 s and scanned the first eight angles of SUR1. SUR2 would occasionally be replaced with a user-defined RHI scan during active convection, so SUR2 scans are not present in every 12-minute scanning period. Both types of SUR scans were interpolated onto a 1 km × 1 km Cartesian grid with 0.5 km vertical grid spacing up to 22 km.

2.3 Storm Tracking

To track precipitating systems using the radar data, we use version 1.4.2 of the Tracking and Object-based Analysis of Clouds (tobac) Python package due to its unique ability to work with any variable on any grid (Heikenfeld et al. 2019). We detect precipitating systems at 4 km above ground level (AGL) during "PRE"-CIP using a reflectivity threshold of 15 dBZ, a minimum pixel threshold of 15, and a minimum distance between features of 15 km. We apply a Gaussian filter with a standard deviation of 0.25, which minimally smooths the reflectivity data yet retains distinct storm boundaries. The combination of these thresholds and filtering reduces the identification of small, isolated pixels and mountain clutter. The precipitating systems at each time step are then linked together using a predictive linking technique, in which tobac uses the previous time step to predict the motion of the current time step, then searches for the system center within a 10-km radius of the predicted center location. If no center is found, the storm track ends at the previous time step. If more than one center is identified, then tobac uses the predictive linking technique to associate each center to its respective storm track. An example of storm tracks from the Black Hollow flash flood-producing storm on 20 July 2021 is shown in Figure 2.1.

Tracked storms with 0-min lifetimes were removed since they all occurred between 1320 LT 2 May 2021 and 1844 LT 4 May 2021 when stratiform precipitation was located directly over

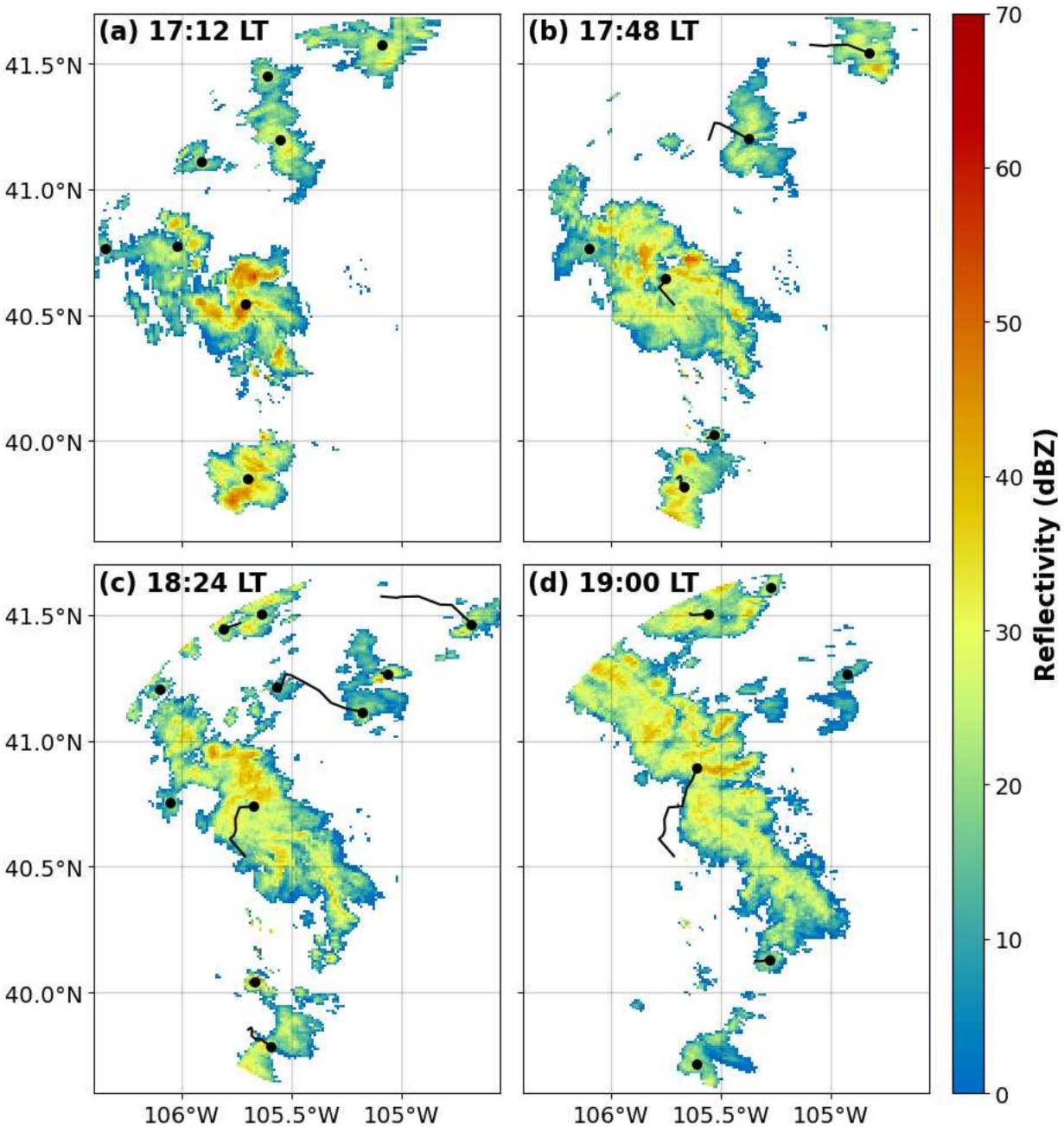

Figure 2.1: Example of the feature detection and storm tracking abilities of tobac at 4 km AGL during the Black Hollow flash flood-producing storm over the Rocky Mountains on 20 July 2021. Black points represent the storm center at the current time step and black lines show the storm track up to the current time step. Storms are colored by reflectivity (dBZ) using the Python ARM Radar Toolkit (Py-ART; Helmus and Collis 2016).

CHIVO. During this time, tobac struggled to link the precipitating systems due to the change in the cone of silence area between SUR1 and SUR2 scans. With a larger cone of silence in SUR2 scans due to less elevation angles scanned, more reflectivity data was removed, so tobac failed to track some system centers over the cone of silence in some time steps. Precipitating systems not located over the cone of silence were retained since they had lifetimes greater than 0 min and their reflectivity areas were unaffected by the changing cone of silence size.

To associate the rain rate field with the precipitating systems identified through reflectivity, tobac uses a two-dimensional watershedding technique to determine an area around the precipitating system center that meets a minimum threshold in a process called segmentation. In this case, this threshold is $R = 0.2$ mm h^{-1}, which corresponds with $Z = 15$ dBZ (or $Z_h = 31.62$ mm^6 m^{-3}) in Equation 2.1. Mean rain rates are calculated for each precipitating system by taking the mean of the rain rates retrieved from the segmentation step. Mean rain rates along each storm track are calculated similarly by taking the mean of the rain rates retrieved from the segmentation step for all precipitating systems along the identified track. Whereas precipitating systems are detected at 4 km AGL, rain rates are retrieved from 3 km AGL to minimize beam blockage from the Rocky Mountains and ice contamination above and within the melting level. Since the recent release of tobac version 1.5.1 made three-dimensional storm tracking possible, we will use three-dimensional radar data in future work to detect storm volumes, which will be more representative of the precipitating system sizes than a vertical slice at 4 km AGL alone.

2.4 Storm Mode Identification

Although tobac allows for the two-dimensional detection of the general precipitation over northern Colorado, different thresholds are required for the three-dimensional identification of the TRMM-heritage storm modes. The first step in storm mode identification is to detect all precipitation features (PFs), which are contiguous echoes greater than 0 dBZ in the composite reflectivity from 3 to 5 km AGL, as was used by Rocque et al. (2024a, manuscript submitted to *J. Geophys. Res.: Atmos.*) and Rocque et al. (2024b, manuscript submitted to *Mon. Wea. Rev.*) in subtropical

South America. To ensure that isolated radar echoes and mountain clutter are not identified, PFs must further have a minimum echo top height of 3 km and minimum area of 4 km^2. Reflectivity data are used to separate PF echoes into stratiform and convective echoes using the methods of Steiner et al. (1995), in which reflectivity values of 40 dBZ or greater are automatically identified as convective echoes, while reflectivity values lower than 40 dBZ must exceed the background reflectivity averaged across an 11-km radius by a threshold based on a function of the area-averaged background reflectivity. The radius of the convective area is also determined by the area-averaged background reflectivity. Echoes that do not meet these convective thresholds and are at least 0 dBZ are then identified as stratiform. Convective and stratiform areas within PFs that are identified by the Steiner et al. (1995) convective-stratiform separation method are then categorized into the four TRMM-heritage storm modes using the moderate thresholds defined in Houze et al. (2015):

- Deep convective cores (DCCs) are three-dimensional contiguous echoes of 30 dBZ with core echo top heights of at least 8 km.
- Wide convective cores (WCCs) are three-dimensional contiguous echoes of 30 dBZ with a horizontal extent of at least 800 km^2.
- Deep and wide convective cores (DWCCs) are three-dimensional contiguous echoes of 30 dBZ that satisfy both the DCC and WCC thresholds.
- Broad stratiform regions (BSRs) are three-dimensional contiguous stratiform echoes with a horizontal extent of at least 10,000 km^2. The size requirement was reduced from 30,000 km^2 (Houze et al. 2015) to 10,000 km^2 in this study given the size of the CHIVO radar domain considered herein.

Similar to the storm tracking methodology, rain rates are retrieved from 3 km AGL as a compromise between beam blockage along the high terrain at lower vertical levels and the presence of frozen hydrometeors at higher vertical levels.

Chapter 3

Overview of the Synoptic Environment

3.1 Moisture

Figure 3.1 shows Hovmöller diagrams depicting the diurnal cycle of specific humidity and specific humidity anomalies over 100°W to 110°W for the months of May, June, July, and August 2021. During all four months of the "PRE"-CIP field project, a gradient of specific humidity values was primarily centered over the eastern slopes of the Rocky Mountains, with lower values located over the high terrain and higher values located to the east over the plains (Figs. 3.1a,c,e,g). However, this gradient deviated from its location toward the east between 08 and 17 local time (LT), which may be due to diabatic heating, eastward storm propagation, or some combination of both. If convection initiated on a given day, it likely developed over the Rockies in the morning and propagated eastward into regions of higher specific humidity over the plains during the afternoon and early evening. The westward retreat of the moisture gradient begins around local sunset (18 LT), thereby marking the return of diabatic cooling that stabilizes the location of the moisture gradient overnight. This west-to-east propagation is similar to the behavior of the thermally driven mountain-plains solenoidal circulation that has been well documented within the Rocky Mountain region (Toth and Johnson 1985; Tripoli and Cotton 1989a,b; Wolyn and McKee 1994; Trier et al. 2010).

Although the specific humidity gradient behaves similarly among all four months in 2021, the values of specific humidity differ greatly. The highest moisture availability east of the Rocky Mountains as well as domain-wide occurred in July (Fig. 3.1e), followed by August (Fig. 3.1g), June (Fig. 3.1c), and May (Fig. 3.1a). Nevertheless, it is difficult to determine the impact of these values without considering their comparison with the historical record. Whereas the strongest specific humidity anomalies occurred east of the mountains during July (Fig. 3.1f), the second strongest positive anomalies in this region happened during May (Fig. 3.1b), followed by June

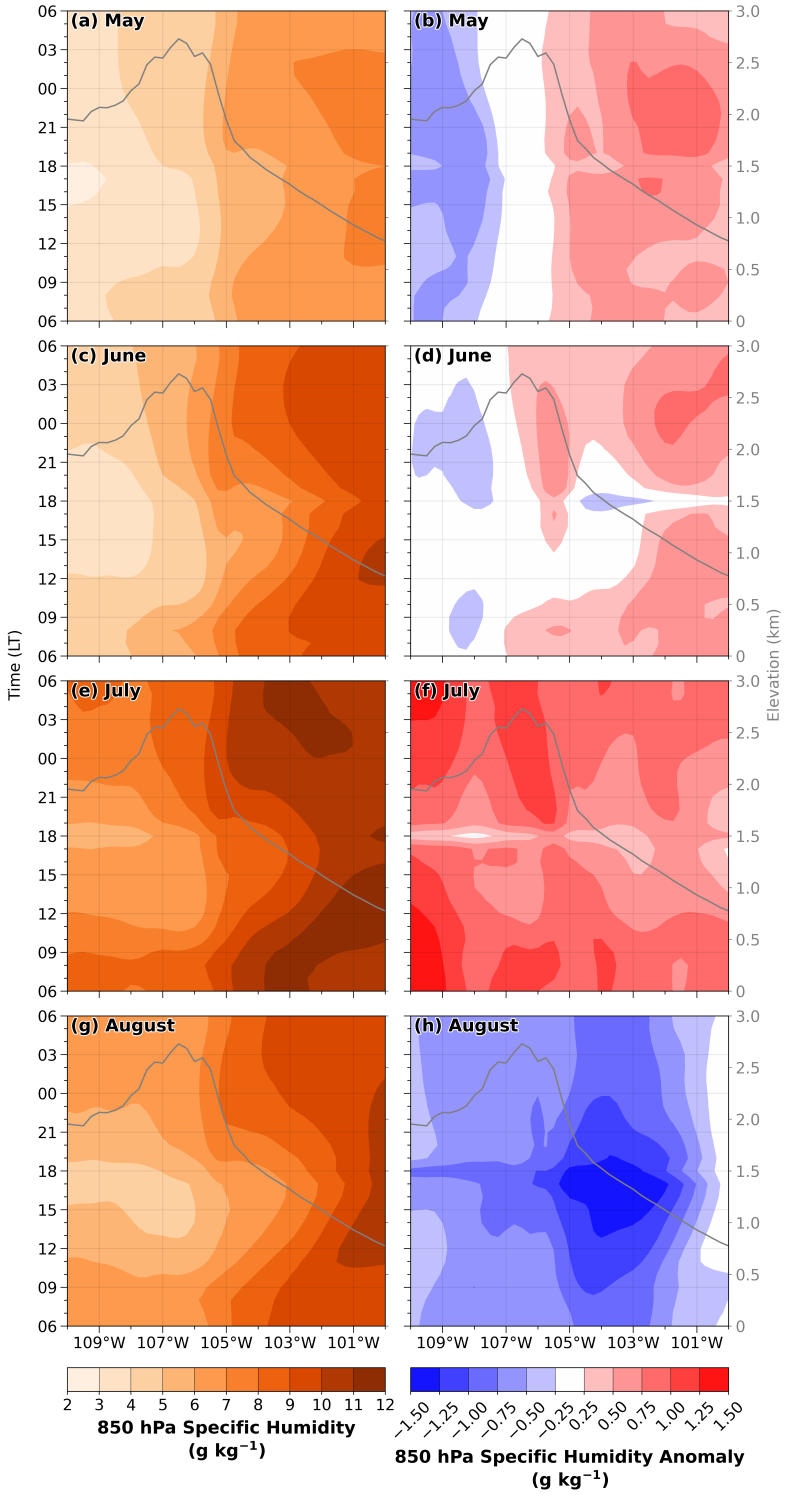

Figure 3.1: Hovmöller diagrams of 850 hPa specific humidity (g kg^{-1}; left) and specific humidity anomalies (g kg^{-1}; right) for the months of (a-b) May, (c-d) June, (e-f) July, and (g-h) August. Anomalies are calculated by subtracting the mean values of 1979–2020 from the 2021 values. The Hovmöller diagrams span 100–110°W and values are averaged across 37–43°N. Times are shown from 06 to 06 local time (LT). The gray contour represents the latitudinally averaged terrain height (km).

(Fig. 3.1d). The strongest positive specific humidity anomalies during these three months occurred around 19 LT, after the westward retreat of the moisture gradient. These late evening and nighttime pockets of positive anomalies hint that moisture transport via the LLJ may have been anomalously strong during these three months. In contrast, August had negative moisture anomalies domain-wide, with the strongest negative values occurring east of the Rocky Mountains between 13 and 19 LT (Fig. 3.1h). Given that August and June possessed comparable values of specific humidity east of the mountains during 2021, the strongly negative moisture anomaly during August hints that convection may have been more suppressed in August than in June, particularly during the afternoon and evening hours when the moisture gradient is still propagating eastward.

3.2 Meridional Wind

The Hovmöller diagrams of meridional wind speed in Figure 3.2 show a strong southerly wind maximum east of the Rocky Mountains around 101°W, with winds increasing in strength around 18 LT, peaking around midnight, and decreasing an hour or two after local sunrise (06 LT). This pattern confirms the presence of the LLJ east of the Rockies during all four months of "PRE"-CIP (Bonner 1968), with the LLJ being the weakest in May (Fig. 3.2a) and strengthening with each successive month (Figs. 3.2b–d). The timing of the LLJ overlaps with the return of moisture to the mountains (Figs. 3.1a,c,e,g), indicating that the southerly winds of the LLJ reintroduce moisture into the higher terrain overnight. Meridional wind speed anomalies (not shown) are all positive east of the Rocky Mountains between 18 and 06 LT, resulting in an anomalously strong LLJ across all months. The meridional wind anomaly in May is not only the strongest of all months, but it is also strong across all other hours of the day. The mean geopotential height (not shown) over the domain during May is 5734 m, which is 154 m lower than the mean over the three summer months, indicating that late spring extratropical cyclones and their frontal systems likely explain the strongly positive meridional wind anomalies seen in May. Pairing the anomalously high moisture availability (Figs. 3.1b,d,f) with an anomalously strong LLJ east of the Rockies (Fig. 3.2)

enhances the southerly transport of warm, moist air from the Gulf of Mexico in all months except for August, which was characterized by anomalously low specific humidity (Fig. 3.1h).

3.3 Vertical Moisture Flux

Another important ingredient to consider is vertical moisture flux wq, one of the key ingredients in Equation 1.2. Negative values of vertical moisture flux, which represent rising motion, occur during the daytime between 10 and 19 LT over the mountains and persist until 00 LT over the plains (Fig. 3.3). This difference in timing between the mountains and plains suggests that although storm initiation is supported by rising motion in the early afternoon everywhere in northern Colorado, rising motion over the plains continues into the night. Between 21 LT and 09 LT, sinking motion, represented by positive anomalies of vertical moisture flux, is prominent over the Rocky Mountains, particularly over the foothills at 105°W. May (Fig. 3.3a) features the weakest sinking motion, July (Fig. 3.3c) has the strongest sinking motion, and the magnitudes of sinking motion in June (Fig. 3.3b) and August (Fig. 3.3d) fall in between. Whereas the magnitude of these positive anomalies across all four months are likely modulated by the amount of moisture present (Figs. 3.1a,c,e,g), the daytime rising and nighttime sinking of moist air over the Rocky Mountains is likely associated with the mountain-plains solenoidal circulation. This circulation is known to have upslope flow during the daytime that transitions to a downslope flow overnight, hence promoting convective initiation over the mountains during the day and over the plains at night (Toth and Johnson 1985; Tripoli and Cotton 1989a,b; Wolyn and McKee 1994; Trier et al. 2010).

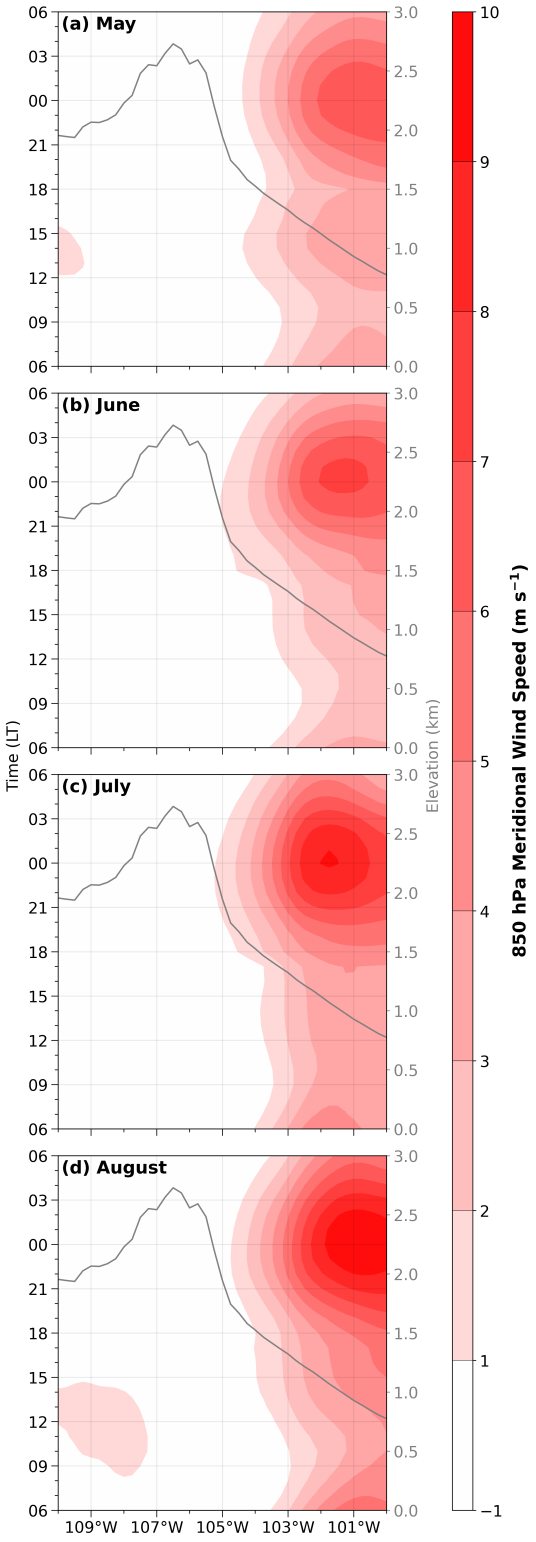

Figure 3.2: Hovmöller diagrams of 850 hPa meridional wind speed (m s^{-1}) for the months of (a) May, (b) June, (c) July, and (d) August 2021. The Hovmöller diagrams span 100–110°W and values are averaged across 37–43°N. Times are shown from 06 to 06 local time (LT). The gray contour represents the latitudinally averaged terrain height (km).

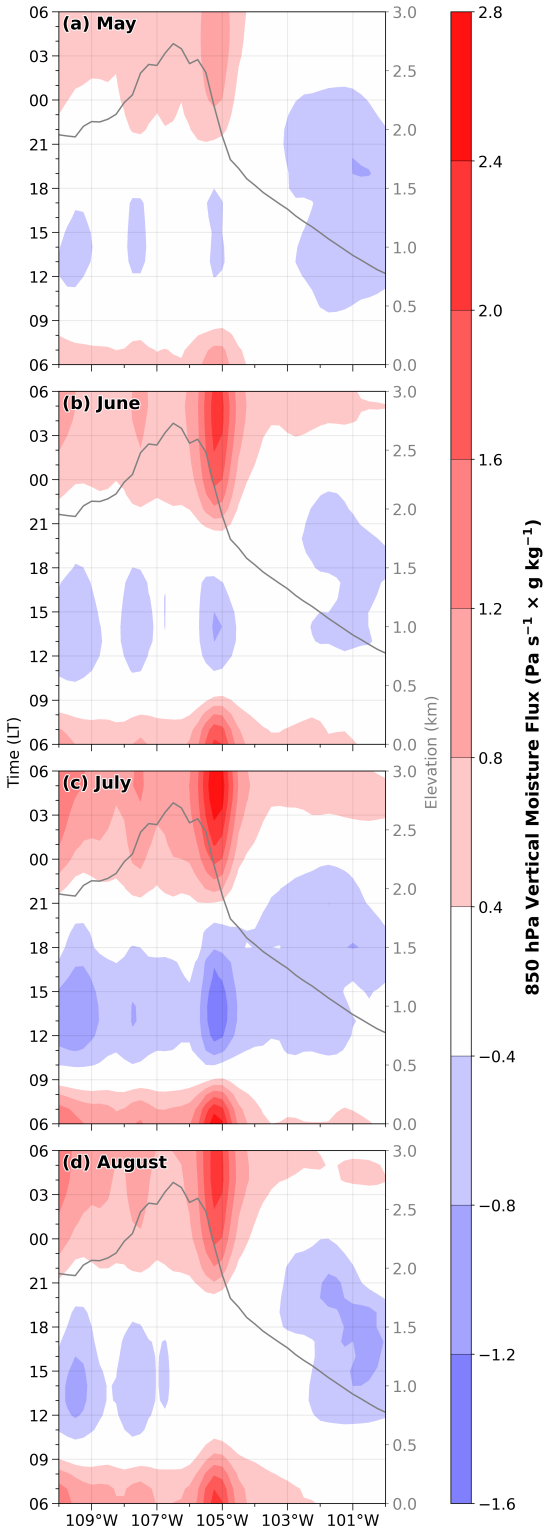

Figure 3.3: Hovmöller diagrams of 850 hPa vertical moisture flux (wq; Pa s^{-1} × g kg^{-1}) for the months of (a) May, (b) June, (c) July, and (d) August 2021. The Hovmöller diagrams span 100–110°W and values are averaged across 37–43°N. Times are shown from 06 to 06 local time (LT). The gray contour represents the latitudinally averaged terrain height (km).

Chapter 4

Overview of the Radar-observed Rainfall

The rainfall observed by CHIVO is represented as a time series of maximum area, mean rain rate, and mean volumetric rain rate as shown in Figures 4.1, 4.2, and 4.3, respectively. May and July feature the most precipitating systems, whereas June and August did not produce as many storms. The high storm production in May coincides with the late spring synoptic-scale forcing, presence of the LLJ, and anomalously high moisture east of the Rockies discussed in Chapter 3. Similarly, the high number of precipitating systems observed in July coincides with the ERA5 data, which showed that July had the second-strongest LLJ (Fig. 3.2c) and both the highest specific humidity values and specific humidity anomalies (Figs. 3.3e,f) of all four months.

May (Fig. 4.1a) features some of the largest storms during "PRE"-CIP, particularly at the beginning and end of the month, further implicating the influence of large-scale systems on northern Colorado rainfall. In contrast, the months of June (Fig. 4.1b), July (Fig. 4.1c), and August (Fig. 4.1d) generally do not feature storms with areas as large as those in May, and they do not persist as long as those in May. This pattern suggests that the diurnal cycle is driving storms in the three summer months rather than large-scale systems. The occurrence of a few large storms in summer, such as those in early and late July and early August, implies that storms initiated in response to the diurnal cycle grew upscale into larger, longer-lived MCSs. May also had the largest mean rain rates (Fig. 4.2a), which is likely an artifact of larger storm areas and thus a larger areal extent for calculating mean rain rates across the domain. The precipitating systems in the three summer months share similar values of mean rain rates, which are weaker than those seen in mid-May (Figs. 4.2b–d).

The highest values for both maximum area and mean rain rate favor storms produced in the late spring month of May, during which synoptic-scale systems influence local rainfall. To examine the overall hydrological impact from all precipitating systems, we use mean volumetric rain rate, which is the product of maximum area and mean rain rate. Volumetric rain rate is an important

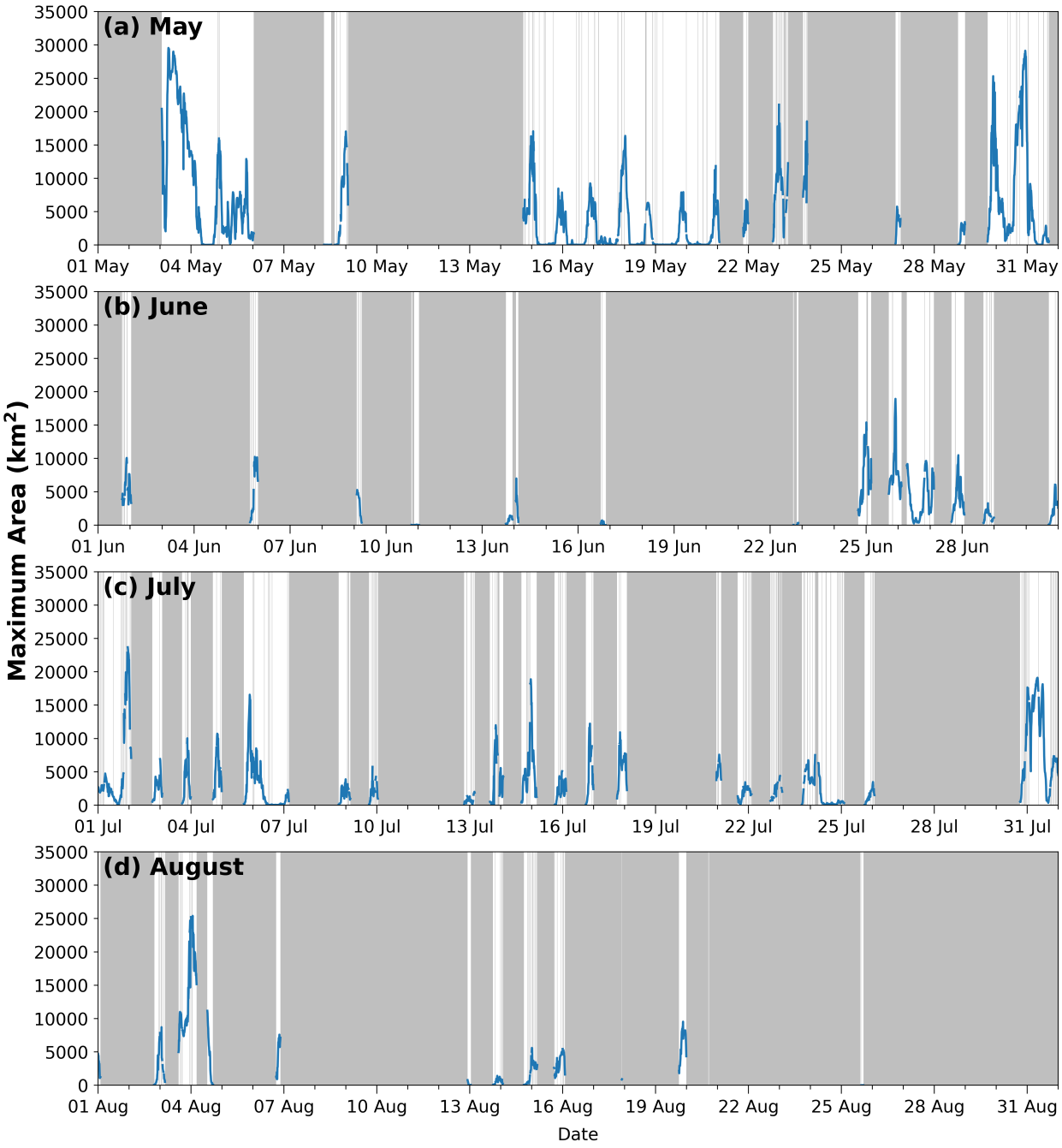

Figure 4.1: Time series of the maximum PF area (km^2) at each radar time step for (a) May, (b) June, (c) July, and (d) August 2021. The gray blocks indicate times that either CHIVO was not operating or did not observe a PF.

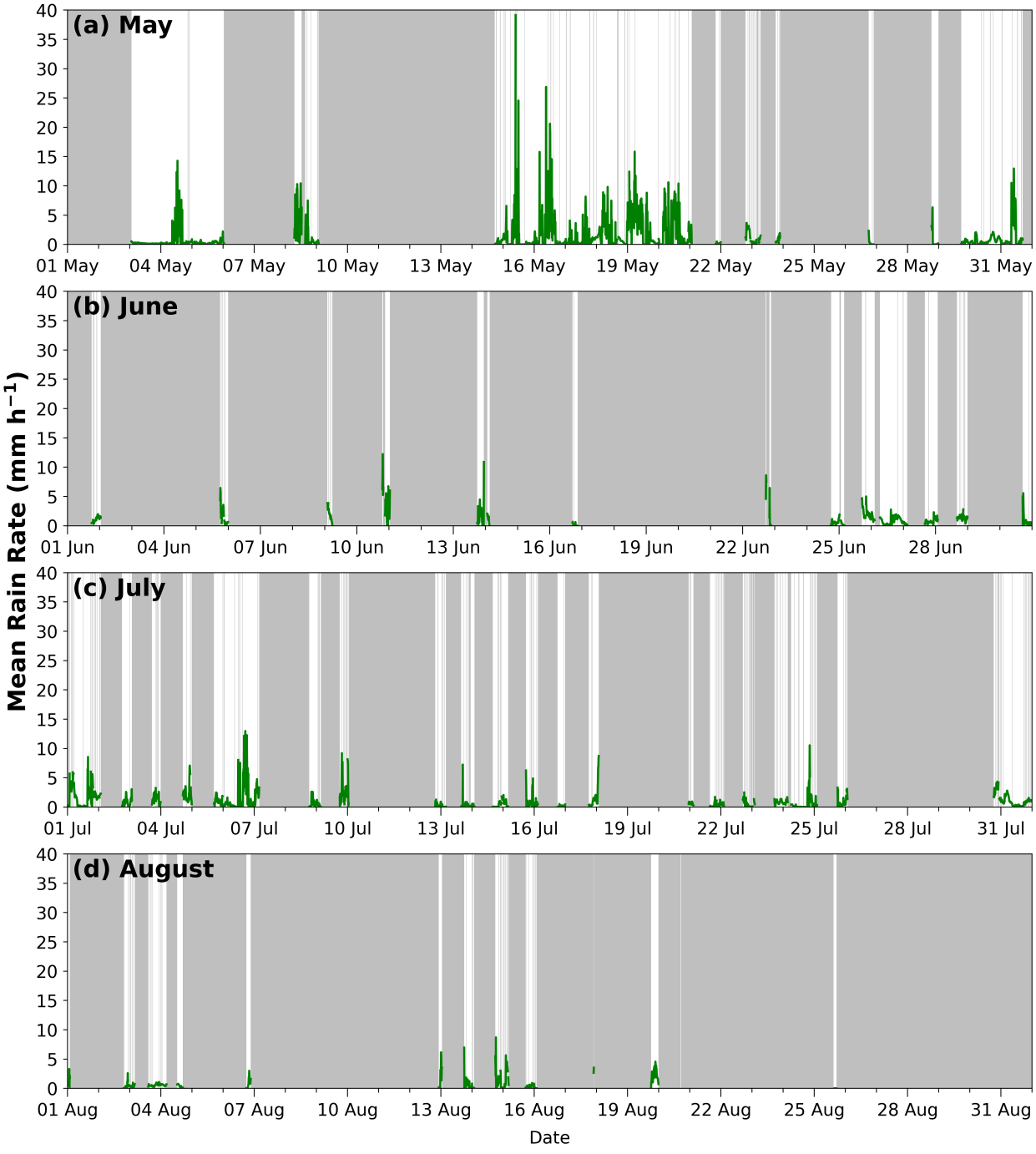

Figure 4.2: Time series of the highest PF mean rain rate (mm h^{-1}) at each radar time step for (a) May, (b) June, (c) July, and (d) August 2021. The gray blocks indicate times that either CHIVO was not operating or did not observe a PF.

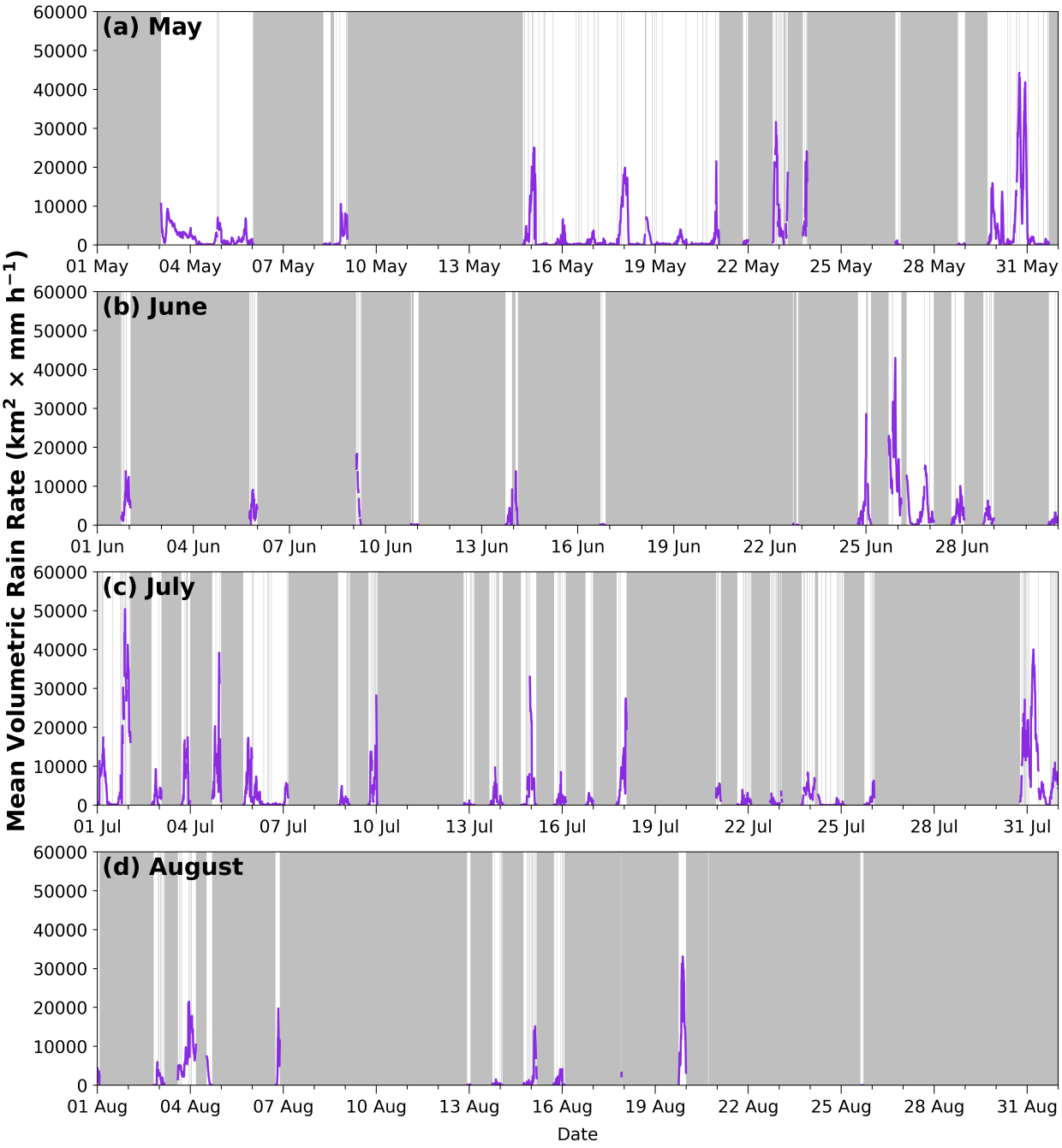

Figure 4.3: Time series of the highest PF mean volumetric rain rate ($km^2 \times mm\ h^{-1}$) at each radar time step for (a) May, (b) June, (c) July, and (d) August 2021. The gray blocks indicate times that either CHIVO was not operating or did not observe a PF.

rainfall metric because it normalizes the observed rainfall by reducing the impact of area and rain rate extremes. This effect is seen in Fig. 4.3, in which the large storms in early May with seemingly large mean rain rates do not possess the largest mean volumetric rain rates. While the large storms in late May retain a high mean volumetric rain rate, other rainfall events with high volumetric rain rates become prominent in late June and early and late July. Therefore, using mean volumetric rain rate highlights both synoptically and diurnally forced events as the most hydrologically significant heavy rainfall-producing events. One such event on 1 July 2021 produced the highest mean volumetric rain rate observed during "PRE"-CIP, during which a back-building MCS formed over the plains and produced 1-h rainfall amounts of 3 to 4 in. in Greeley, CO (Nicholson 2021).

Chapter 5

Storm Tracking

5.1 Spatial Frequency of Storm Occurrence

Now that we know the temporal distribution of precipitating systems in northern Colorado during "PRE"-CIP, it is important to understand where these storms occur spatially, particularly in relation to the Front Range. As was described in Chapter 2, a storm tracking tool called tobac is used to track ground-based radar echoes during the 2021 "PRE"-CIP field experiment. Figure 5.1 shows storm track density plots for all durations (Fig. 5.1a), the shortest-lived storms ($D \leq$ 1 h; Fig. 5.1b), the longest-lived storms ($D >$ 3 h; Fig. 5.1d), and storms with durations in between the short- and long-lived categories (Fig. 5.1c). Although storm tracks are present across the entire CHIVO domain, the highest density of storm tracks is over the Rocky Mountains, especially within the 3-km terrain contour. When separating these precipitating systems by track lifetime, the high-density signal over the Rockies remains regardless of storm duration, suggesting that the higher elevations enhance the occurrence of storms in northern Colorado. Furthermore, 84.1% (4959/5896) of all storm tracks have lifetimes up to at least 1 h, indicating that most of the warm-season precipitation in northern Colorado is short-lived.

Given the dominance of short-lived precipitating systems in northern Colorado, it is essential to understand where these storms initiate and terminate. Figure 5.2 shows the initiation and termination points of all storms. Again, we observe that the highest density of both storm initiation and termination occurs over the Rocky Mountains, particularly around the 3-km terrain height. The high-density signals over the high terrain in Figures 5.1 and 5.2 suggest that convection is primarily forced by the diurnal cycle and mountain processes like the mountain-plains solenoidal circulation rather than synoptic-scale ascent, which is weak in the summer due to the absence of strong temperature gradients. Although it is unknown during what month each of these precipi-

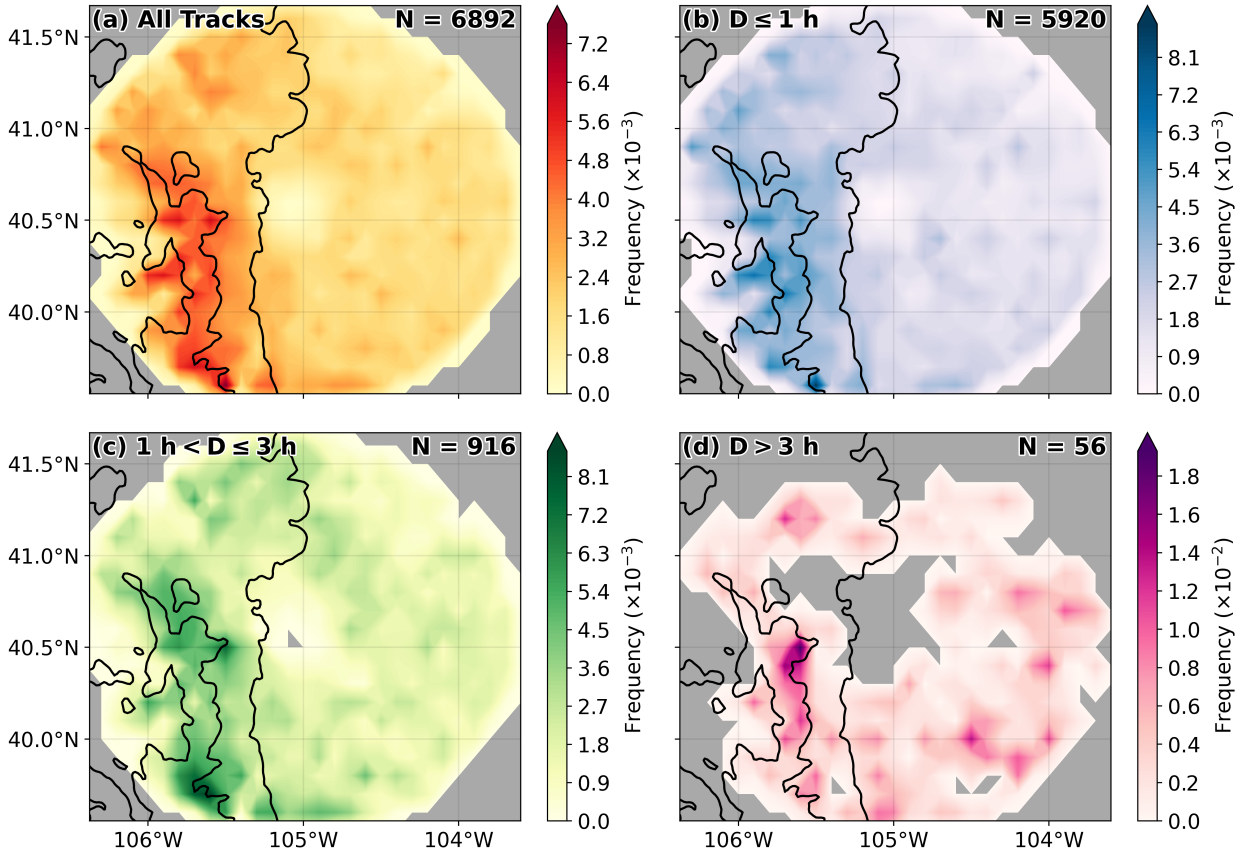

Figure 5.1: Spatial distribution of tobac-identified storm frequency for (a) all durations, (b) durations 1 h or less, (c) durations greater than 1 h and up to and including 3 h, and (d) durations greater than 3 h. N is the number of storms in each duration category. The north–south-oriented black contour represents the 2-km terrain height, while all other black contours represent the 3-km terrain height. The black cross is the location of the CHIVO radar.

tating systems occur, this result agrees with the strong presence of the diurnal cycle discussed in Chapter 3, as well as the diurnal pulsing of rainfall discussed in Chapter 4.

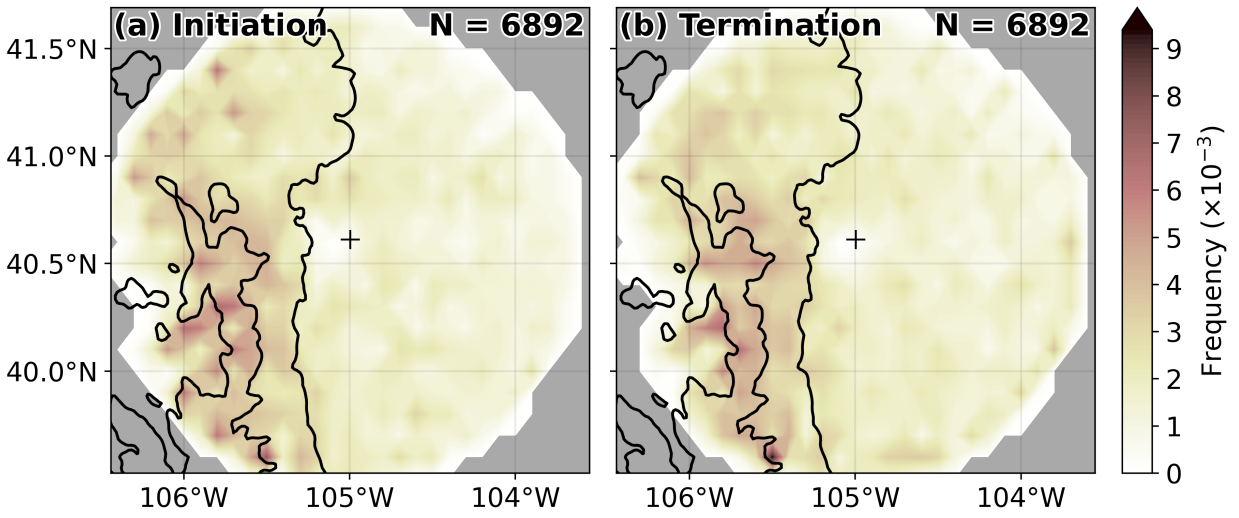

Figure 5.2: Spatial distribution of tobac-identified storm frequency for storm (a) initiation and (b) termination locations. N is the number of storms in each duration category. The north–south-oriented black contour represents the 2-km terrain height, while all other black contours represent the 3-km terrain height. The black cross is the location of the CHIVO radar.

5.2 Intensity-duration Phase Space

Now that we have information about the lifetimes of tracked storms over northern Colorado, we can calculate the mean rain rate of these storms to fill out the intensity-duration phase space (Fig. 1.1) with real observations. Figure 5.3 visualizes this intensity-duration framework as a two-dimensional histogram, with intensity represented by the mean rain rate (mm h^{-1}) along a storm track on the vertical axis and storm duration (h) represented on the horizontal axis. There are a few high-intensity, low-duration storm tracks and a few low-intensity, high-duration tracks. The former are associated with young, vigorous convection, like DCCs, whereas the latter represent matured, developed precipitating systems, like BSRs (Houze et al. 2015). However, these two locations on the phase space do not have the highest density of storm track counts. We already knew about the dominance of short-lived storms from previous figures, but Figure 5.3 shows that most storm

tracks fall within the low-intensity, short-duration bins. That is, precipitation in northern Colorado is generally characterized by short-lived, weak storms.

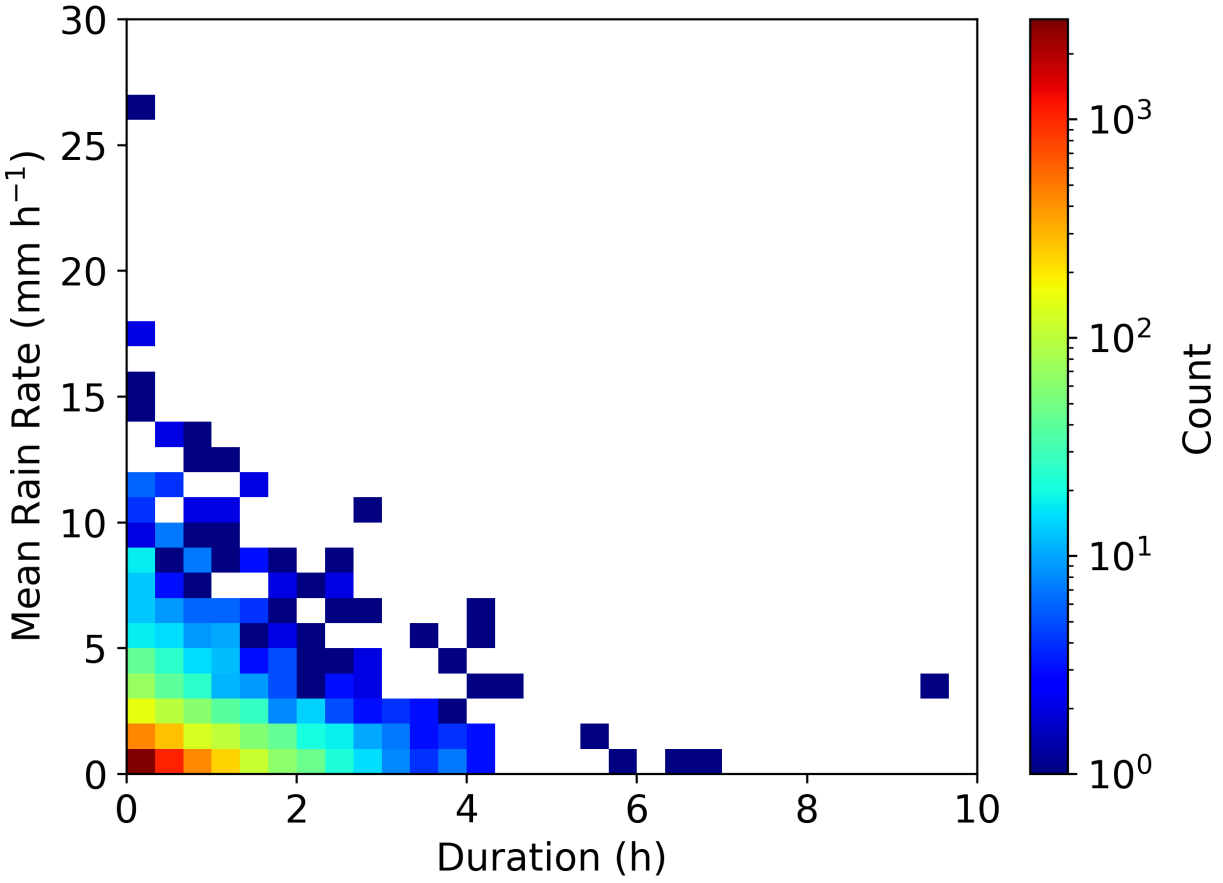

Figure 5.3: Two-dimensional histogram of the mean rain rate (1 mm h^{-1} bins) along a storm track versus the duration (20 min bins) of that track.

Chapter 6

Storm Modes

Since tobac did not have the ability to track objects in three-dimensional space at the time this research was conducted, the TRMM-heritage storm modes that rely upon three-dimensional echoes for identification are not tracked. Therefore, the following discussion considers storm modes as individual objects, such that multiple storm modes may be identified during one radar time step, and a new set of storm modes are identified in the next time step.

6.1 Temporal and Spatial Occurrence of Storm Modes

Akin to the time series of storm characteristics in Chapter 4, Figure 6.1 shows the number of PFs, DCCs, DWCCs, and BSRs observed on a given day of the field project. Overall, 174,432 PFs (Fig. 6.1a) were observed during "PRE"-CIP. Among storm modes, there were 15,263 DCCs (Fig. 6.1b), 13 DWCCs (Fig. 6.1c), and 716 BSRs (Fig. 6.1d) observed. Note that the absence of WCCs does not mean broader convection was not observed, but rather that it was also deep and thus fit the DWCC criteria. PFs show the general occurrence of precipitation during the field project, with the highest number of events occurring in May and July. These events coincide with the presence of synoptic-scale forcing seen in the ERA5 Hovmöller diagrams during May as well as the strong moisture and meridional wind anomalies seen in July, as discussed in Chapter 3.

DCCs also occur nearly throughout the entire field campaign, most notably in July and August, when moisture availability was the highest during the field project (Fig. 3.1). DWCCs only occurred across four time periods, with the highest number occurring in early July and early August. Finally, BSRs are most frequent throughout the month of May, with the highest number occurring in early and late May, whereas the rest of the BSRs intermittently occur across late June, early and mid-July, and early August. This peak occurrence in May is, again, likely associated with the stronger synoptic-scale forcing during that time compared with the three summer months. Not only

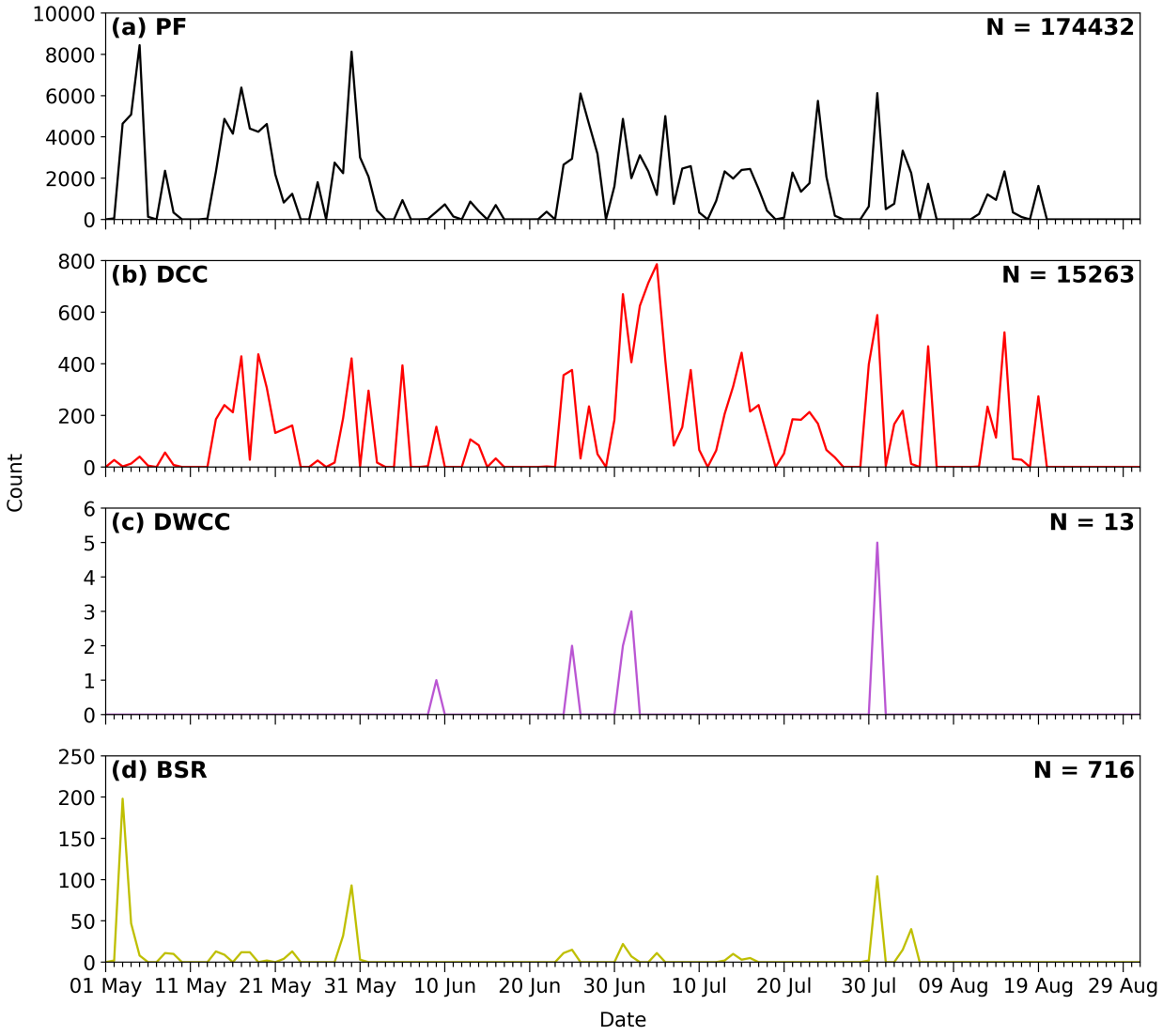

Figure 6.1: Times series of the daily count of (a) PFs, (b) DCCs, (c) DWCCs, and (d) BSRs between May and August 2021. N is the sample number of PFs and each storm mode.

is deep convection the most dominant storm mode in northern Colorado, but broader convective or stratiform rain does not occur without the presence of DCCs.

Spatially, PFs and the three storm modes occur over different regions in northern Colorado. Although PFs (Fig. 6.2a) and DCCs (Fig. 6.2b) span nearly the entire radar domain, their highest occurrence is over the Rocky Mountains, particularly around the 3-km terrain contours. DWCCs occur primarily over the plains (Fig. 6.2c), and BSRs are mostly in the foothills and plains (Fig. 6.2d). This limited extent of BSRs past the foothills is an artifact of both the 10,000 km^2 area threshold for BSRs and CHIVO's 125-km range. Nevertheless, the highest concentration of DCCs over the mountains and DWCCs and BSRs over the foothills and plains suggests that the storm modes may follow a life cycle, like that discussed in Romatschke and Houze (2010), Rasmussen and Houze (2011), Houze et al. (2015), and Rasmussen et al. (2016). That is, although DCCs occur everywhere over the radar domain, those that initiate over the higher terrain or foothills may broaden into DWCCs and then weaken into BSRs over the plains with eastward propagation during the convective life cycle associated with MCSs.

6.2 Diurnal and Topographic Influences on Storm Modes

Hovmöller diagrams of the three storm modes in Figure 6.3 provide further evidence for a storm mode life cycle in northern Colorado. DCCs (Fig. 6.3a) exhibit three possibilities for storm occurrence and propagation: (1) DCCs initiate over the Rocky Mountains and possess little-to-no storm movement, (2) DCCs initiate over the Rocky Mountains close to the foothills and propagate eastward over the plains, and (3) DCCs initiate over the plains and propagate eastward. The highest frequency of DCCs occurs between 12 and 15 LT and over the high terrain, falling within the first scenario. Since DCCs in the intensity-duration framework are thought of as high-intensity, low-duration storms, the high concentration of DCCs over the Front Range agrees with the tobac results regarding the high concentration of short-lived precipitating systems in the same location. DWCCs (Fig. 6.3b) occur between 15 and 00 LT over the plains, later than and eastward of the

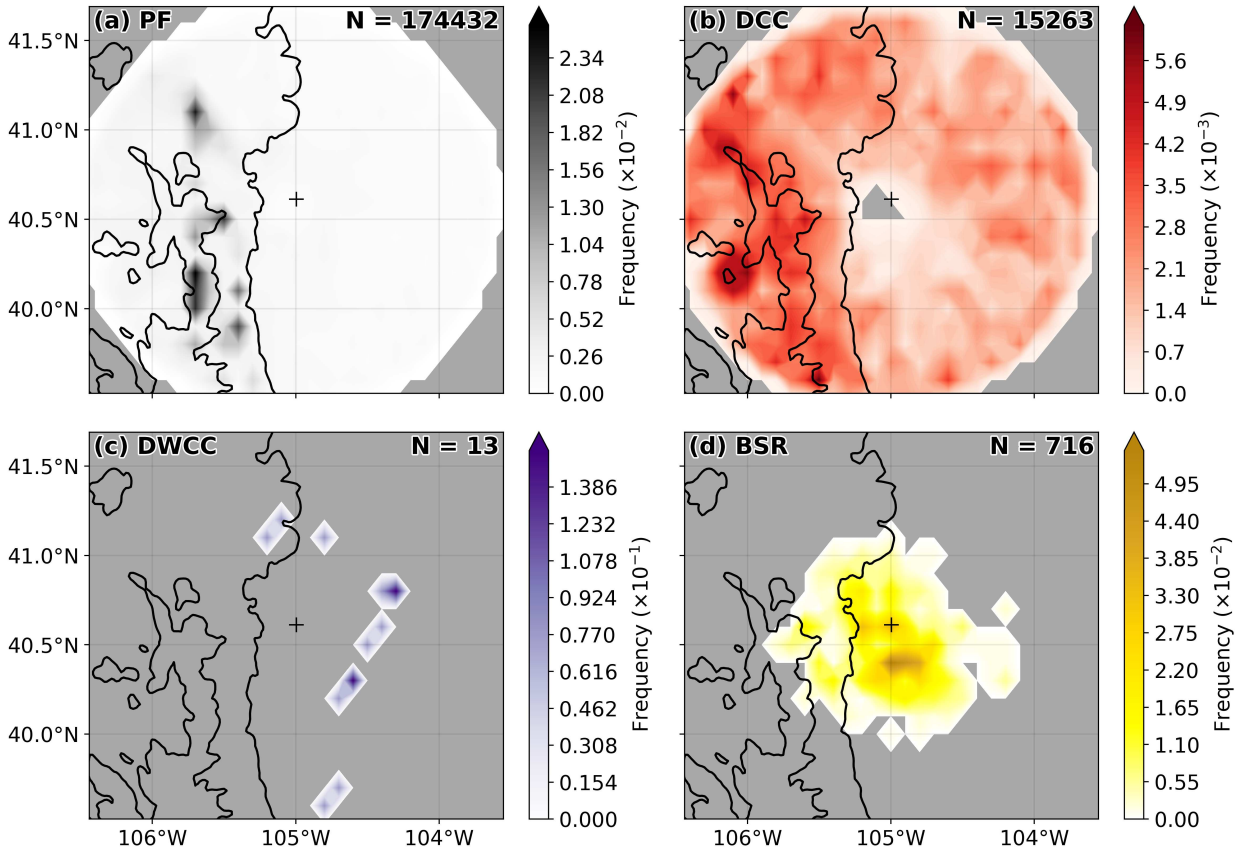

Figure 6.2: Spatial distribution of TRMM-heritage storm mode frequency for (a) PFs, (b) DCCs, (c) DWCCs, and (d) BSRs. N is the sample number of PFs and each storm mode. The north–south-oriented black contour represents the 2-km terrain height, while all other black contours represent the 3-km terrain height. The black cross is the location of the CHIVO radar.

DCC maximum. However, due to the low number of DWCC samples, no definitive life-cycle connection can be made between the two deep convective modes.

BSRs (Fig. 6.3c) occur at all times of the day around the foothills, but the maximum frequency signature is prominent between 14 and 20 LT and has a slight eastward propagation. A secondary maximum in BSR frequency is centered around the foothills and occurs much earlier, between 09 and 12 LT. The timing and longitudinal extent of the maximum frequency of DCCs and BSRs suggests that some DCCs initiate over the Rocky Mountains and weaken and grow upscale into BSRs as they propagate eastward over the plains. Moreover, the afternoon maximum in DCCs over the mountains coincides with the upslope vertical moisture flux seen in the ERA5 Hovmöller diagrams (Fig. 3.3), indicating that the mountain-plains solenoidal circulation drives convective initiation in northern Colorado during the warm season. Meanwhile, those DCCs that initiate or propagate over the plains are supported by the eastward propagating moisture gradient (Fig. 3.1) and the downslope branch of the mountain-plains solenoid that becomes prominent in the late evening.

Figure 6.4 shows the frequency of occurrence of PFs, DCCs, and BSRs in the 12 h before (negative time) and 12 h after (positive time) the hours of maximum mean rain rate and mean volumetric rain rate. With the hour of maximum mean rain rate occurring at 04 LT, the maximum frequency of PFs, DCCs, and BSRs is offset by 9 to 11 h (Fig. 6.4a). This offset indicates that intensity alone in the intensity-duration framework is not enough to characterize the rainfall observed over the Front Range. In contrast, when the hour of maximum mean volumetric rain rate occurs at 18 LT, PF occurrence maximizes 4 to 6 h prior, DCC occurrence maximizes 3 to 5 h prior, and BSR occurrence maximizes 1 h prior (Fig. 6.4b). That is, as PFs initiate and intensify into DCCs, mean volumetric rain rate increases. As DCCs then weaken and broaden into BSRs and propagate eastward, the loss of intensity but gain in length scale L leads to an increase on the duration axis and, hence, a peak in the mean volumetric rain rate. Therefore, considering the entire intensity-duration phase space and not one axis alone allows for a better understanding of how the spectrum of storm modes physically relates to heavy rainfall.

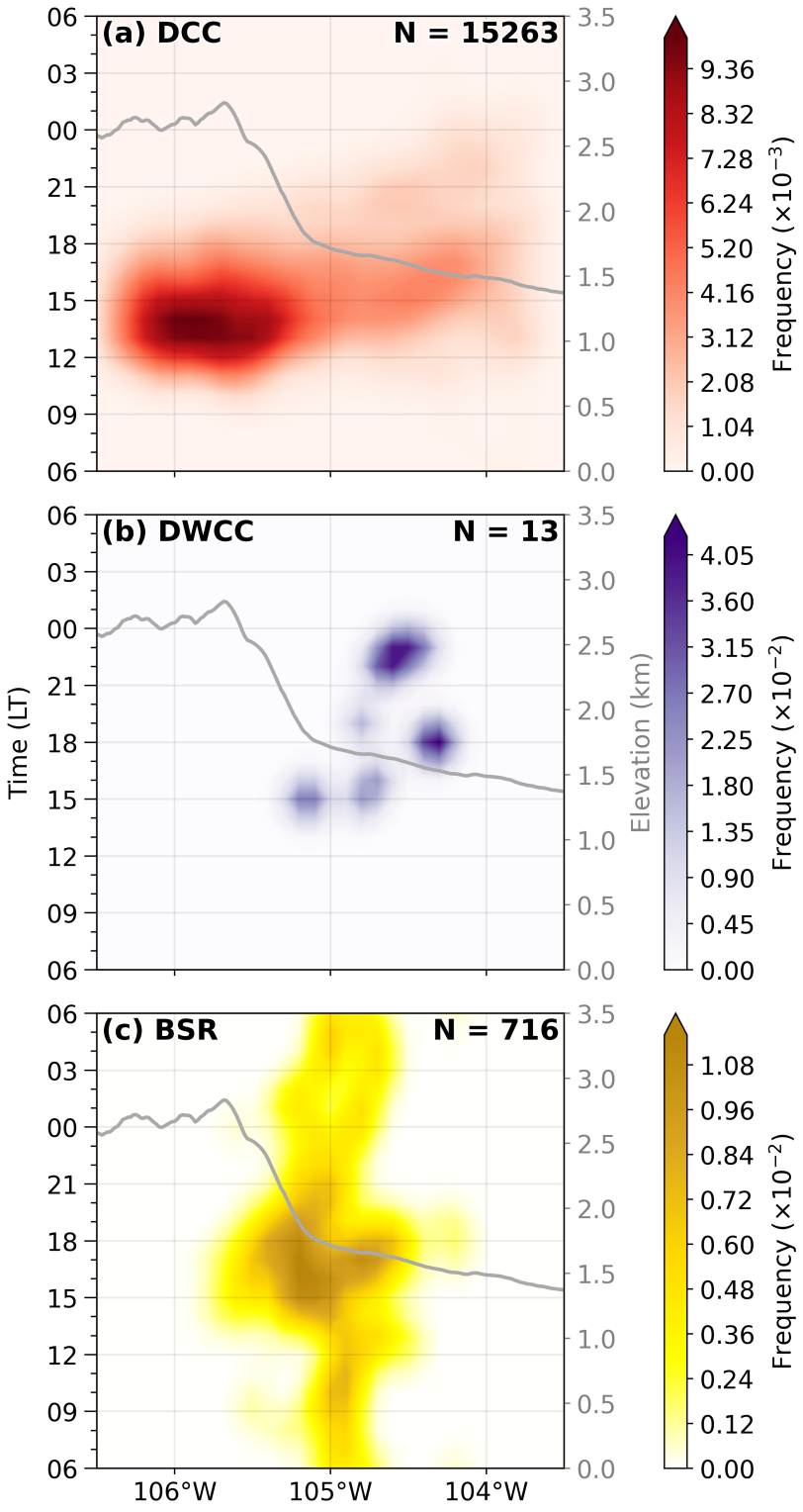

Figure 6.3: Hovmöller diagrams of (a) DCC, (b) DWCC, and (c) BSR frequency. The Hovmöller diagrams span 103.5–106.5°W and values are averaged across 39.0–42.5°N. Times are shown from 06 to 06 local time (LT). The gray contour represents the latitudinally averaged terrain height. N is the number of samples of each storm mode.

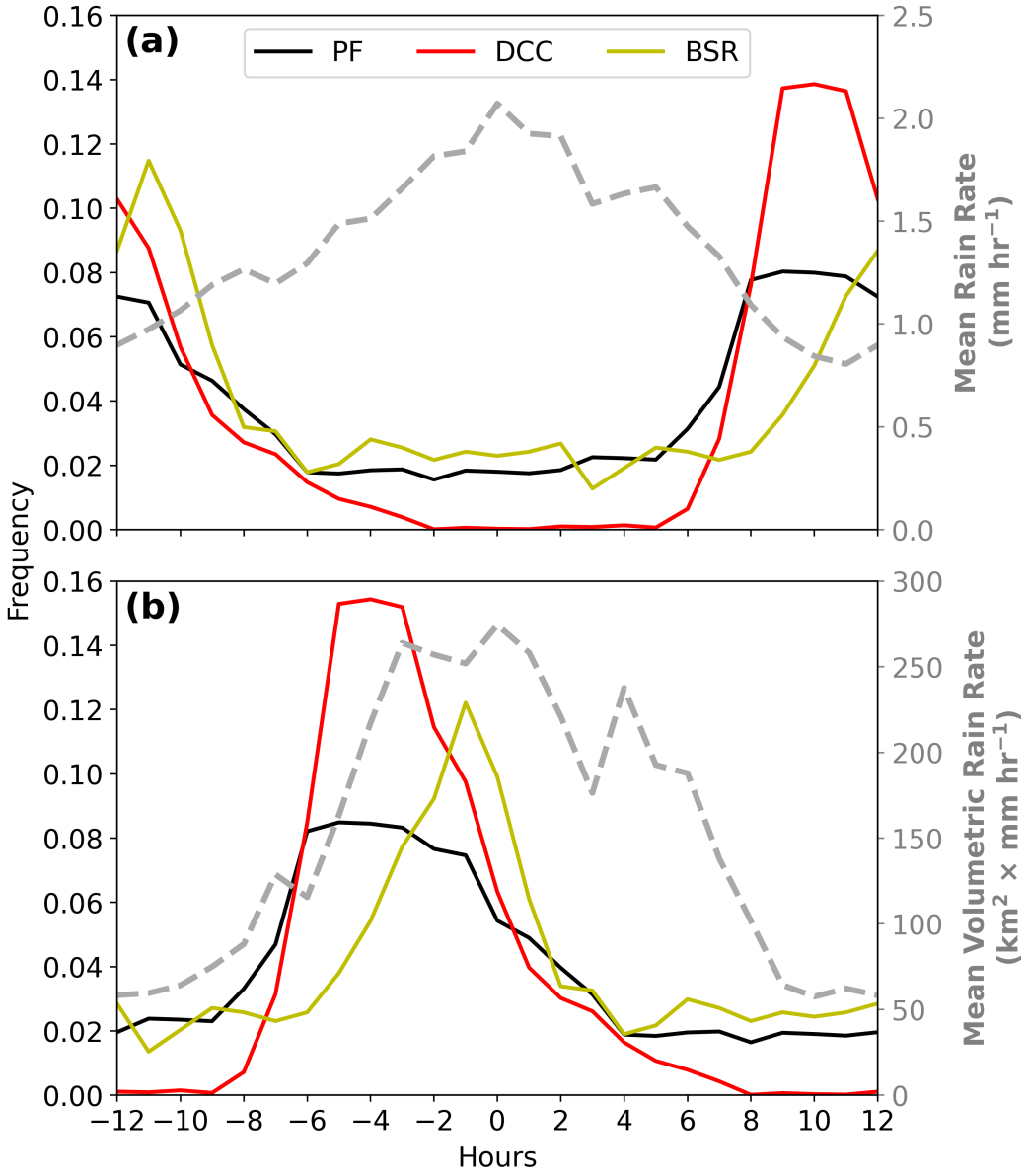

Figure 6.4: Frequency of occurrence of PFs (black), DCCs (red), and BSRs (yellow) for the 12 hours before (negative time) and after (positive time) the hours of maximum (a) mean rain rate (04 LT; mm h^{-1}; dashed gray) and (b) mean volumetric rain rate (18 LT; km^2 × mm h^{-1}; dashed gray). DWCCs are excluded due to their low sample number.

6.3 Vertical Structure of Storm Modes

To further support the presence of a storm mode life cycle in northern Colorado, contoured frequency-by-altitude diagrams (CFADs) show how the vertical structure of PFs and storm modes changes with height. Since storm modes are identified through reflectivity thresholds, the CFADs in Figure 6.5 use reflectivity to represent vertical structure. PFs (Fig. 6.5a) and BSRs (Fig. 6.5d) share similar vertical structures, generally having reflectivity values up to 30 dBZ and vertical extents up to 12 km. The region of maximum frequency for both PFs and BSRs encompasses reflectivity values between 5 and 25 dBZ and vertical heights between 6 and 8 km. The similarities in vertical structural between BSRs and PFs indicate that PFs are largely composed of stratiform rain, even though the sample number of BSRs is over 240 times fewer than that of PFs.

Similarities in vertical structure can also be seen with DCCs (Fig. 6.5b) and DWCCs (Fig. 6.5c), which reach echo top heights of at least 14 km. The high-reflectivity core for DCCs is around 35 to 40 dBZ and is located in between 3 and 7 km, whereas the high-reflectivity core for DWCCs occupies a slightly wider range of reflectivity values from 35 to 45 dBZ and is located between 2 and 6 km. The deep convective storm modes are expected to share similar vertical structures due to not only the low sample number of DWCCs, but also the fact that DWCCs are a subset of DCCs, but with wider convective cores. Furthermore, the deep convective storm modes have higher echo top heights, narrower high-reflectivity cores, and higher reflectivity values in the high-reflectivity core than the stratiform echoes. This distinction between deep convection and stratiform rain supports the notion of a life cycle from DCCs to BSRs, such that DCC reflectivity cores weaken and widen and echo top heights become shallower as convection grows upscale.

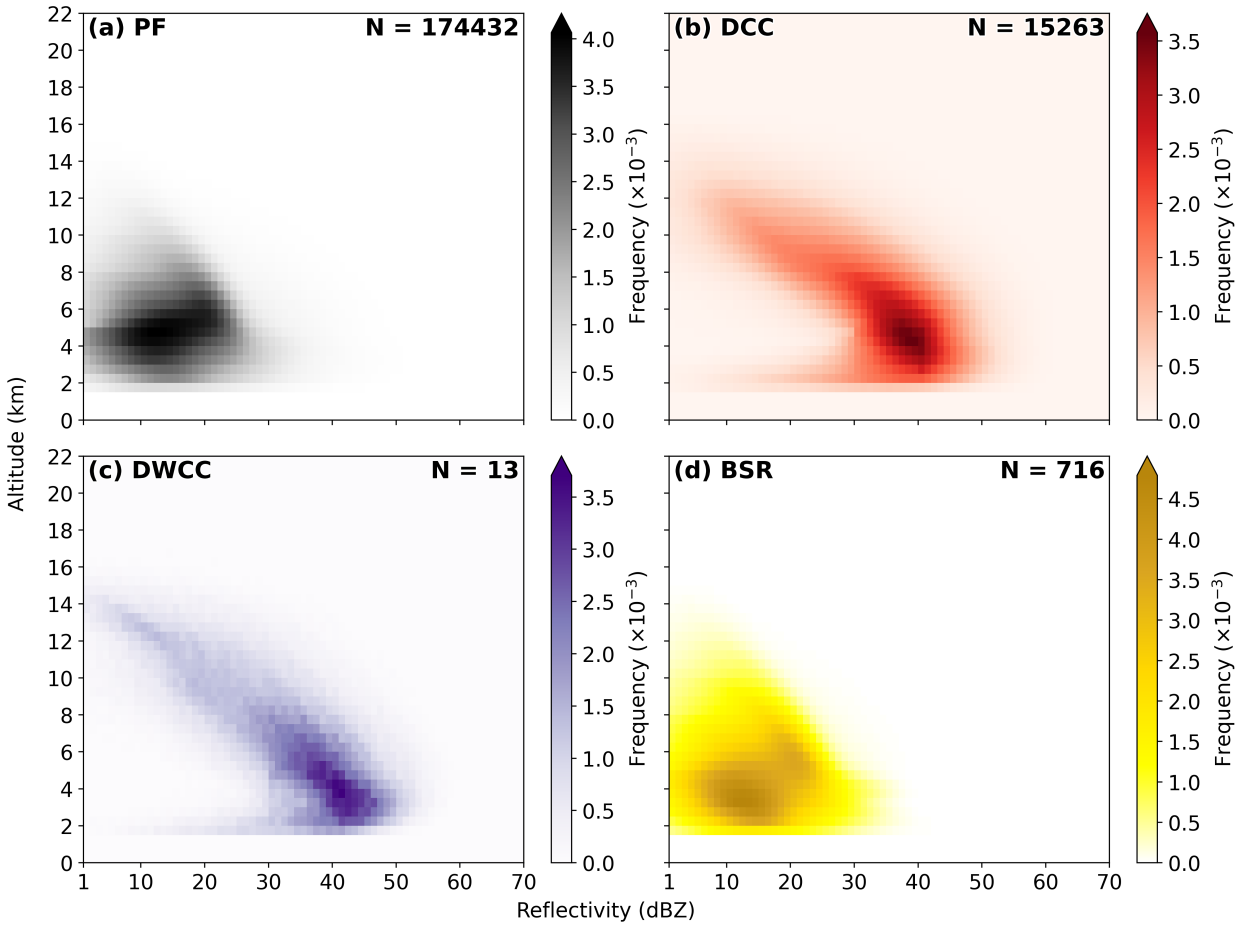

Figure 6.5: Contoured frequency-by-altitude diagrams (CFADs; 0.5 km altitude bins) of reflectivity (1 dBZ bins) for (a) PFs, (b) DCCs, (c) DWCCs, and (d) BSRs. N is the number of samples of PFs and each storm mode.

Chapter 7

Conclusions and Future Work

This investigation provides insight into the topographic and diurnal influences on the storm mode climatology of northern Colorado using four months of reanalysis data and ground-based research radar data from the 2021 Preparatory Rockies Experiment for the Campaign in the Pacific ("PRE"-CIP). To contextualize the field project, we used 850 hPa specific humidity, meridional wind speed, and vertical moisture flux from the fifth-generation European Centre for Medium-Range Weather Forecasts (ECMWF) reanalysis (ERA5) dataset (Hersbach et al. 2022) between May and August 2021. There is an overnight specific humidity gradient over the foothills of the Rocky Mountains that propagates eastward in response to the diabatic heating of the eastward-facing slopes and/or latent heat release of initial convection after sunrise; this moisture gradient retreats westward after sunset. This behavior is likely caused by the thermally driven mountain-plains solenoidal circulation, which is the primary driver of convection in the Rocky Mountains in the absence of strong synoptic forcing (Toth and Johnson 1985; Tripoli and Cotton 1989a,b; Wolyn and McKee 1994; Trier et al. 2010). July has both the largest specific humidity values and anomalies, followed by June and May. The moisture values in August compare with those in June, but the anomalies for August are negative throughout the domain, indicating that the anomalously low moisture availability likely suppresses convection.

Meridional wind speed east of the Rocky Mountains captures the nocturnal Great Plains low-level jet (LLJ; Bonner 1968; Mitchell et al. 1995), which increases in magnitude and spatiotemporal extent with each successive month. Although August is characterized by anomalously low moisture, the presence of the strongest LLJ likely enhances nocturnal low-level convergence with downslope flow more than any other month, thereby reducing the magnitude of convective suppression. Upslope vertical moisture flux occurs over the Rockies during the day, whereas moist, downslope flow occurs at night, again showing how strongly the mountain-plains solenoidal circulation influences convective initiation in northern Colorado during the warm season (Toth and

Johnson 1985; Tripoli and Cotton 1989a,b; Wolyn and McKee 1994; Trier et al. 2010). Furthermore, the nocturnal maximum in the LLJ coincides with the anomalously positive vertical moisture flux over the eastern slopes of the Rocky Mountains, suggesting that the convergence of easterly flow from the LLJ with downslope flow from the mountain-plains solenoidal circulation is a mechanism for reinvigorating and sustaining nighttime convection.

Due to the ability of the Tracking and Object-based Analysis of Clouds (tobac) Python package to work with any variable on any grid (Heikenfeld et al. 2019), tracking precipitation within the domain of the Colorado State University C-band Hydrological Instrument for Volumetric Observation (CHIVO) allows us to retrieve storm intensity and duration information in accordance with the ingredients-based framework of Doswell et al. (1996). For precipitating systems with a radar reflectivity threshold of 15-dBZ, their highest frequency is over the Front Range, especially the 3-km terrain contours, whether the storms are short-lived ($D \leq 1$ h), long-lived ($D > 3$ h), or some duration in between (1 h $\leq D < 3$ h). The initiation and termination locations of these precipitating systems also exhibit a similar pattern, in which the highest concentration of points for both storm initiation and termination is over the mountains. The similarities between the short-duration and initiation and termination high-frequency locations indicates that not only are short-lived storms dominant, but they are largely influenced by orographic lifting over the terrain. While short-lived precipitating systems are prominent, constituting over 80% of the rainfall-producing population, so are small mean rain rates. That is, short-lived and weak storms are the most common precipitating system type in the Rockies.

However, in terms of the extreme precipitation features (PFs) associated with heavy rainfall-producing storms, deep convection is the dominant storm mode, with 15,263 deep convective cores (DCCs), 13 deep and wide convective cores (DWCCs), and 716 broad stratiform regions (BSRs) identified. Like general precipitation from tobac, PFs and DCCs also achieve a maximum frequency over the Front Range. The maximum in DWCC frequency is over the plains, whereas the maximum in BSR frequency is over the foothills. Moreover, DCCs peak in the afternoon over the mountains, either (1) initiating and remaining quasi-stationary over the terrain, (2) initiating over

the terrain and propagating eastward over the plains, or (3) initiating and propagating eastward over the plains. This afternoon maximum coincides with the upslope vertical moisture flux observed over the Front Range in the ERA5 data, suggesting that the mountain-plains solenoid drives the development of warm-season deep convection in northern Colorado. BSRs peak in frequency in the foothills in the late afternoon to late evening hours and feature limited eastward propagation due to the area threshold for BSRs and the limited range of the CHIVO radar. Although the timing and location between DCCs and BSRs indicates a life cycle from deep convection over the high terrain to stratiform precipitation over the plains, DWCCs peak between the evening and nighttime hours, after the BSR maximum frequency. This offset is likely due to the low sample number of DWCCs.

The hour of maximum mean rain rate occurs at 04 LT, which is 9 to 11 h offset from the maximum frequency of PF and storm mode occurrence. Such a large offset indicates that intensity alone is insufficient for relating the storm modes to rainfall characteristics. By incorporating area to calculate mean volumetric rain rate, we find that the hour of maximum mean volumetric rain rate occurs at 18 LT, which is just 3 to 5 h after the DCCs maximize their frequency over the mountains and 1 h after BSRs maximize their frequency over the foothills. Therefore, volumetric rain rate is a better descriptor of overall rainfall in the Rocky Mountains because it encompasses both axes of the intensity-duration phase space rather than just one. The vertical structure of storm modes further supports the convective life cycle since deep convection has higher echo tops and stronger and narrower reflectivity cores than its stratiform counterparts. Even though general precipitation is best characterized by short-lived and light rain-producing storms, deep convection constitutes the vast majority of heavy rainfall-producing storms.

The ultimate goal of the "PRE"-CIP 2021 field project is to be a complementary dataset to the original PRECIP 2022 field project, whereby we can apply the exact same storm tracking and storm mode identification to the research radars deployed to Taiwan and Japan. Located in the western Pacific Ocean, Taiwan experiences a variety of synoptic-scale events that influence local precipitation, such as the quasi-stationary Mei-yu front in the late spring and early summer (Chen 1983;

Kuo and Chen 1990; Chen et al. 2007) and southwesterly monsoonal flow and tropical cyclones in the warm season (Chen et al. 2007; Jou et al. 2011; Wu et al. 2017). The interaction of these synoptic-scale events with the high terrain of the nearly north–south-oriented Central Mountain Range, comparable in height to the Colorado Rocky Mountains, can lead to orographically enhanced heavy rainfall events over Taiwan (Kuo and Chen 1990; Chen et al. 2007; Jou et al. 2011; Xu et al. 2012; Wu et al. 2017). With the information from the ground-based research radars stationed in Taiwan and Japan during the 2022 Prediction of Rainfall Extremes Campaign in the Pacific (PRECIP), we can ultimately compare how storm modes differ between moisture-limited (Colorado) and moisture-rich environments (Taiwan and Japan), thereby improving our global understanding of the commonalities of heavy rainfall-producing storms.

Bibliography

Ashley, S. T., and W. S. Ashley, 2008: Flood fatalities in the United States. *J. Appl. Meteor. Climatol.*, **47**, 805–818, https://doi.org/10.1175/2007JAMC1611.1.

Banta, R. M., and C. B. Schaaf, 1987: Thunderstorm genesis zones in the Colorado Rocky Mountains as determined by traceback of geosynchronous satellite images. *Mon. Wea. Rev.*, **115**, 463–476, https://doi.org/10.1175/1520-0493(1987)115<0463:TGZITC>2.0.CO;2.

Bonner, W. D., 1968: Climatology of the low level jet. *Mon. Wea. Rev.*, **96**, 833–850, https://doi.org/10.1175/1520-0493(1968)096<0833:COTLLJ>2.0.CO;2.

Caracena F., R. A. Maddox, L. R. Hoxit, and C. F. Chappell, 1979: Mesoanalysis of the Big Thompson storm. *Mon. Wea. Rev.*, **107**, 1–17, https://doi.org/10.1175/1520-0493(1979)107<0001:MOTBTS>2.0.CO;2.

Chen, C.-S., Y.-L. Chen, C.-L. Liu, P.-L. Lin, and W.-C. Chen, 2007: Statistics of heavy rainfall occurrences in Taiwan. *Wea. Forecasting*, **22**, 981–1002, https://doi.org/10.1175/WAF1033.1.

Chen, G. T.-J., 1983: Observational aspects of the Mei-yu phenomenon in subtropical China. *J. Meteor. Soc. Japan*, **61**, 306–312, https://doi.org/10.2151/jmsj1965.61.2_306.

Cifelli, R., V. Chandrasekar, S. Lim, P. C. Kennedy, Y. Wang, and S. A. Rutledge, 2011: A new dual-polarization radar rainfall algorithm: Application in Colorado precipitation events. *J. Atmos. Oceanic Technol.*, **28**, 352–364, https://doi.org/10.1175/2010JTECHA1488.1.

Doswell, C. A., III, H. E. Brooks, and R. A. Maddox, 1996: Flash flood forecasting: An ingredients-based methodology. *Wea. Forecasting*, **11**, 560–581, https://doi.org/10.1175/1520-0434(1996)011<0560:FFFAIB>2.0.CO;2.

Fritsch, J. M., R. J. Kane, and C. R. Chelius, 1986: The contribution of mesoscale convective weather systems to the warm-season precipitation in the United States. *J. Climate Appl. Meteor.*, **25**, 1333–1345, https://doi.org/10.1175/1520-0450(1986)025<1333:TCOMCW>2.0.CO;2.

Gochis, D., and Coauthors, 2015: The Great Colorado Flood of September 2013. *Bull. Amer. Meteor. Soc.*, **96**, 1461–1487, https://doi.org/10.1175/BAMS-D-13-00241.1.

Haberlie, H. M., and W. S. Ashley, 2019: A radar-based climatology of mesoscale convective systems in the United States. *J. Climate*, **32**, 1591–1601, https://doi.org/10.1175/JCLI-D-18-0559.1.

Heikenfeld, M., P. J. Marinescu, M. Christensen, D. Watson-Parris, F. Senf, S. C. van den Heever, and P. Stier, 2019: Tobac 1.2: Towards a flexible framework for tracking and analysis of clouds in diverse datasets. *Geosci. Model Dev.*, **12**, 4551–4570, https://doi.org/10.5194/gmd-12-4551-2019.

Helmus, J. J., and S. M. Collis, 2016: The Python ARM Radar Toolkit (Py-ART), a library for working with weather radar data in the Python programming language. *J. Open Res. Software*, **4**, e25, https://doi.org/10.5334/jors.119.

Hersbach, H., and Coauthors, 2022: ERA5 monthly averaged data on pressure levels from 1940 to present. Copernicus Climate Change Service (C3S) Climate Data Store (CDS), accessed 17 November 2022, https://doi.org/10.24381/cds.6860a573.

Houze, R. A., Jr., D. C. Wilton, and B. F. Smull, 2007: Monsoon convection in the Himalayan region as seen by the TRMM Precipitation Radar. *Quart. J. Roy. Meteor. Soc.*, **133**, 1389–1411, https://doi.org/10.1002/qj.106.

——, K. L. Rasmussen, M. D. Zuluaga, and S. R. Brodzik, 2015: The variable nature of convection in the tropics and subtropics: A legacy of 16 years of the Tropical Rainfall Measuring Mission satellite. *Rev. Geophys.*, **53**, 994–1021, https://doi.org/10.1002/2015RG000488.

Jou, B. J.-D., W.-C. Lee, and R. H. Johnson, 2011: An overview of SoWMEX/TiMREX. *The Global Monsoon System: Research and Forecasts*, 2nd ed. Chang C.-P., Ed., World Scientific, 303–318, https://doi.org/10.1142/9789814343411_0018.

Kuo, Y.-H., and G. T.-J. Chen, 1990: The Taiwan Area Mesoscale Experiment (TAMEX): An overview. *Bull. Amer. Meteor. Soc.*, **71**, 488–503, https://doi.org/10.1175/1520-0477(1990)071%3C0488:TTAMEA%3E2.0.CO;2.

Maddox, R. A., L. R. Hoxit, C. F. Chappell, and F. Caracena, 1978: Comparison of meteorological aspects of the Big Thompson and Rapid City flash floods. *Mon. Wea. Rev.*, **106**, 375–389, https://doi.org/10.1175/1520-0493(1978)106<0375:COMAOT>2.0.CO;2.

Mitchell, M. J., R. W. Arritt, and K. Labas, 1995: A climatology of the warm season Great Plains low-level jet using wind profiler observations. *Wea. Forecasting*, **10**, 576–591, https://doi.org/10.1175/1520-0434(1995)010%3C0576:ACOTWS%3E2.0.CO;2.

Nicholson, K., 2021: Heavy rains prompt flash flood warnings, watches across the Front Range. Greeley Tribune, Accessed 3 May 2022, https://www.greeleytribune.com/2021/07/01/rain-flash-flood-warning-watch-colorado/.

Petersen, W. A., and Coauthors, 1999: Mesoscale and radar observations of the Fort Collins flash flood of 28 July 1997. *Bull. Amer. Meteor. Soc.*, **80**, 191–216, https://doi.org/10.1175/1520-0477(1999)080<0191:MAROOT>2.0.CO;2.

Rasmussen, K. L., and R. A. Houze Jr., 2011: Orogenic convection in subtropical South America as seen by the TRMM satellite. *Mon. Wea. Rev.*, **139**, 2399–2420, https://doi.org/10.1175/MWR-D-10-05006.1.

——, M. M. Chaplin, M. D. Zuluaga, and R. A. Houze Jr., 2016: Contribution of extreme convective storms to rainfall in South America. *J. Hydrometeor.,* **17**, 353–367, https://doi.org/10.1175/JHM-D-15-0067.1.

Romatschke, U., and R. A. Houze Jr., 2010: Extreme summer convection in South America. *J. Climate*, **23**, 3761–3791, https://doi.org/10.1175/2010JCLI3465.1.

——, S. Medina, and R. A. Houze Jr., 2010: Regional, seasonal, and diurnal variations of extreme convection in the South Asian region. *J. Climate*, **23**, 419–439, https://doi.org/10.1175/2009JCLI3140.1.

Schumacher, R. S., and K. L. Rasmussen, 2020: The formation, character and changing nature of mesoscale convective systems. *Nat. Rev. Earth Environ.*, **1**, 300–314, https://doi.org/10.1038/s43017-020-0057-7.

Steiner, M., R. A. Houze Jr., and S. E. Yuter, 1995: Climatological characterization of three-dimensional storm structure from operational radar and rain gauge data. *J. Appl. Meteor.*, **34**, 1978–2007, https://doi.org/10.1175/1520-0450(1995)034%3C1978:CCOTDS%3E2.0.CO;2.

Trier, S., C. Davis, and D. Ahijevych, 2010: Environmental controls on the simulated diurnal cycle of warm-season precipitation in the continental United States. *J. Atmos. Sci.*, **67**, 1066–1090, https://doi.org/10.1175/2009JAS3247.1.

Tripoli, G., and W. Cotton, 1989a: Numerical study of an observed orogenic mesoscale convective system. Part 1: Simulated genesis and comparison with observations. *Mon. Wea. Rev.*, **117**, 273–304, https://doi.org/10.1175/1520-0493(1989)117%3C0273:NSOAOO%3E2.0.CO;2.

——, and ——, 1989b: Numerical study of an observed orogenic mesoscale convective system. Part 2: Analysis of governing dynamics. *Mon. Wea. Rev.*, **117**, 305–328, https://doi.org/10.1175/1520-0493(1989)117<0305:NSOAOO>2.0.CO;2.

Toth, J. J., and R. H. Johnson, 1985: Summer surface flow characteristics over northeast Colorado. *Mon. Wea. Rev.*, **113**, 1458–1469, https://doi.org/10.1175/1520-0493(1985)113<1458:SSFCON>2.0.CO;2.

Wolyn, P., and T. McKee, 1994: The mountain–plains circulation east of a 2-km-high north–south barrier. *Mon. Wea. Rev.*, **122**, 1490–1508, https://doi.org/10.1175/1520-0493(1994)122%3C1490:TMPCEO%3E2.0.CO;2.

Wu, M., C.-C. Wu, T.-H. Yen, and Y. Luo, 2017: Synoptic analysis of extreme hourly precipitation in Taiwan during 2003–12. *Mon. Wea. Rev.*, **145**, 5123–5140, https://doi.org/10.1175/MWR-D-17-0230.1.

Xu, W., E. J. Zipser, Y.-L. Chen, C. Liu, Y.-C. Liou, W.-C. Lee, and B. J.-D. Jou, 2012: An orography-associated extreme rainfall event during TiMREX: Initiation, storm evolution, and maintenance. *Mon. Wea. Rev.*, **140**, 2555–2574, https://doi.org/10.1175/MWR-D-11-00208.1.

Zipser, E. J., D. J. Cecil, C. Liu, S. W. Nesbitt, and D. P. Yorty, 2006: Where are the most intense thunderstorms on Earth? *Bull. Amer. Meteor. Soc.*, **87**, 1057–1071, https://doi.org/10.1175/BAMS-87-8-1057.